




Two-dimensional simulations of flow in ice-covered lakes with horizontal variations in surface albedo

Donovan J. M. Allum ^{*}, Andrew P. Grace , and Marek Stastna 

Applied Mathematics, University of Waterloo, Waterloo Ontario, Canada N2L 3G1



(Received 31 March 2022; accepted 12 August 2022; published 3 October 2022; corrected 19 April 2023)

We present numerical simulations of radiatively driven convection at temperatures below the temperature of maximum density, as observed in ice-covered lakes in early spring. The purpose of these simulations is to isolate the phenomenon of lateral circulation driven by horizontal variations in surface albedo (e.g., due to partial snow cover) in an idealized and simplified system. The system we consider is one with uniform solar radiation except in a small “shadowed” region at the center of the domain which has damped radiation intensity. By comparing cases with and without a shadowed region, we identify gravity currents at the surface flowing away from the shadowed region. Not only do these gravity currents represent a mechanism for lateral transport at the surface below ice cover, but they also act as a catalyst for inducing earlier vertical mixing that develops at a faster rate than the Rayleigh-Taylor-like instabilities which drive vertical convection away from the shadow. To the authors’ knowledge, only bathymetry and wind forcing at the surface have been presented as major mechanisms for lateral circulation in ice-covered lakes, and hence these simulations may provide a hitherto unreported mechanism for inducing lateral circulation.

DOI: [10.1103/PhysRevFluids.7.103501](https://doi.org/10.1103/PhysRevFluids.7.103501)

I. INTRODUCTION

A large number of inland lakes will have some form of ice cover during the winter season [1–3]. More than half are at high latitudes in the Northern Hemisphere [2]. For many arctic lakes, the ice cover is perennial [4]. However, most lakes with any period of ice cover have an ice-free summer with freezing and break up dates at the start and end of winter [1,5,6]. The freezing and break-up dates suggest a transitional period between ice-free and complete cover with a period of incomplete ice cover, with typically more mixing prior to the break-up date compared to just after the freezing date [7]. Even for perennially frozen lakes and lakes past the freezing date, 100% ice coverage is not always expected [1,5,6,8]. Climate change is predicted to continue the observed trend of reducing the time between freezing and break-up dates, as well as increasing the number of break-ups between the freezing date and the break-up date [1,3]. In addition, the number of lakes with perennial ice coverage is decreasing [4]. Incomplete ice cover is present in many inland lakes at different stages of winter and must be considered for a complete understanding of lake dynamics. There are two main consequences of incomplete or variable ice cover: (1) shear wind stress in areas of no ice cover and (2) horizontal variations in incoming solar radiation. In this paper we neglect any wind forcing effects and focus entirely on horizontal variations in solar radiation and the effect it has on temperature distributions in a lake environment.

Increasing temperatures in an ice-covered lake (complete coverage or otherwise) is different than in temperate or tropical lakes because of the nonlinearity of the equation of state for water at low

^{*}dallum@uwaterloo.ca

temperatures. The equation of state has a maximum density at approximately 4°C (T_{MD}). Increasing temperature towards T_{MD} increases density. Hence, if the water is above the bottom of the domain, increasing temperature can generate vertical buoyancy fluxes downwards into the water column [9,10].

In the early winter, after ice-on, the dominant mechanism to increase temperatures in an ice-covered lake is via heat trapped in a sediment bottom boundary over the ice-free season, released in the winter. In this phase of winter (known as Winter I in [11]), the ice is typically covered by a thick layer of snow which deflects and absorbed most incoming solar radiation. This bottom boundary heat flux into the water strengthens the stratification in the lake interior [11]. Once the snow melts, solar radiation is able to penetrate the ice and becomes the dominant temperature forcing mechanism. Due to the inverted equation of state, solar radiation destabilizes the water column from the snow-covered period, leading to the formation of a deepening and warming convective mixed layer (CML) [11–14]. The CML is a region below the surface of an ice-covered lake which is nearly uniform in temperature [11,12,14] which dominates the bulk of the motion in an ice-covered lake. In Refs. [14] and [15], differential heating in the shallow regions was shown to increase the deepening and heating rate of the CML. References [14] and [15] assume a system with $\approx 25\%$ of the domain with a maximum depth smaller than the photic depth. There are many ice-covered lakes where the shallow regions occupy a much smaller fraction of the lake, and, hence, differential heating in shallow regions is expected to be less important and other mechanisms are needed to explain lateral motion under the ice [16–20]. The work herein is concerned with timescales sufficiently long to allow motion due lateral variations in solar radiation to develop. These timescales are much shorter than those required for a complete CML to form. However, there will be definable regions in the vertical with and without convection, and to avoid confusion we refer to the region with convection as the convective layer (CL).

It is well established that lateral variations in temperature—and therefore lateral buoyancy variations—drive lateral motion [13–15,21]. When solar radiation is the main driver of convection, as is the case in the late winter in ice-covered lakes, nonuniform bathymetry generates these lateral buoyancy gradients [14,15]. Wind on ice-free lakes in the winter has also been shown to generate lateral circulation in basin scale simulations [22]. Proper ice-free simulations on the basin scale are especially problematic because the turbulent fluxes between the air-water interface are difficult to resolve [5], without even considering the additional complication of a free boundary surface. Nonuniform intensity of solar radiation can also lead to horizontal buoyancy gradients that will generate lateral motion [21,23,24]. Reference [23] attributes lateral temperature variations and circulation to lateral variations in optical properties and ice depth in a lake in British Columbia. Other research that attempts to quantify lateral variations is rare. The need to explore nonuniform solar radiation intensity as a mechanism for lateral motion is mentioned briefly in a recent review on lake convection [13]. It is also mentioned in a recent paper on differential heating the near shore as an alternative mechanism for horizontal transport to bathymetry variations which is the focus of the paper [15]. Existing research using high-resolution, nonhydrostatic simulations of ice-covered lakes does not consider the effect of horizontal variations in solar radiation [14,15,22], leaving a clear research gap to be explored in this paper.

The primary focus of this process study is to analyze the effect of lateral variations in solar radiation on the time-dependent distribution of temperature in the interior of an ice-covered lake. We also analyze the effect that these lateral variations will have on the distribution of passive tracers to represent material suspended in the water column, like dissolved oxygen or nutrients. We study a two-dimensional system, initially at constant temperature to analyze the general effect of lateral variations in solar radiation intensity at the surface; effectively the simplest possible configuration. We perform parameter variations away from this main system to probe the parameter dependence of the resulting motion in order to establish that our results are representative for a broad range of field situations. The remainder of this paper is organized as follows: a methods section that presents the equations of motion, describes the system and any quantities of interest. A results section follows which first presents a comparison between a case with and without horizontal variations in solar

radiation, then presents the parameter variation analysis, and finally the effect of artificial noise is considered. There is a short discussion section which connects the parameters used herein to measurements in the field. The final section is a brief summary of conclusions and directions for future work.

II. METHODS

A. Equations of motion

We use the nonhydrostatic, pseudospectral model SPINS [25] to solve the stratified, incompressible Navier-Stokes equations under the Boussinesq approximation to simulate the fluid motion induced by horizontal variations in solar forcing:

$$\frac{D\vec{u}}{Dt} = -\frac{1}{\rho_0}\vec{\nabla}p + \nu\nabla^2\vec{u} - g\frac{\rho}{\rho_0}\hat{k}, \quad (1a)$$

$$\vec{\nabla} \cdot \vec{u} = 0, \quad (1b)$$

$$\frac{DT}{Dt} = \kappa_T\nabla^2T + \frac{Q_0}{\lambda}F(x, z). \quad (1c)$$

This model has been previously applied to a wide variety of scenarios to produce accurate, high-resolution simulations [26–29]. Equation (1a) is the momentum equation to determine the fluid velocity, \vec{u} ; Eq. (1b) is the incompressibility condition; Eq. (1c) is the temperature evolution equation. The last term in the temperature equation is the radiative forcing term, the form of which is given in Sec. II B.

The density, ρ , is determined from the temperature via an approximation to the UNESCO equation of state [30], shifted so that the maximum temperature coincides with 4 °C. This shifted equation of state has been previously applied to simulations of cold water convection [28].

In Sec. II B 1 we present the equation of motion and initial conditions for two passive tracers that will be used for the unshadowed and shadowed cases to quantify horizontal transport due to the shadowed region.

This paper’s primary focus is on lateral circulation but it would be useful to also quantify how a shadowed region modulates motion of any kind. In Sec. II B 2 three bulk quantities are presented which will aid in further quantifying the differences between the shadowed and unshadowed cases.

B. System of interest

The system of interest is a subset of the interior of a shallow lake, sufficiently far from any sloping boundaries with complete ice coverage that blocks any mechanical wind forcing at the surface. Initially, the entire domain is set to a constant temperature, T_0 . We neglect the Coriolis force due to the relatively short timescale of $O(10^3$ s) and length scales of $O(1-10$ m) that are relevant to these simulations. A schematic of the system of interest is given in Fig. 1.

We use a rectangular domain in the xz plane with periodic boundary conditions in the horizontal and free-slip boundary conditions in the vertical. Other simulations of ice-covered lakes typically fix the temperature to 0 °C at the surface so that heat is lost via a diffusive boundary layer to the ice [14,15]. We do not include this boundary condition in the present study as our focus is on the dynamics further below. However, it is an avenue for future work. The domain width, L_x , and height, L_z , are given in Table I. There are many different lakes where the study of lateral motion has been conducted [18,19,31]. As such, the simulations presented within are not meant to represent a specific lake. Initially at constant temperature, this system is subjected to constant time solar forcing with spatial variations determined by

$$F(x, z) = \exp\left(-\frac{L_z - z}{\lambda}\right) \left\{ 1 - A_l \exp\left[-\frac{(x - x_s)^{8w_d}}{w_d^{8w_d}}\right] \right\}. \quad (2)$$

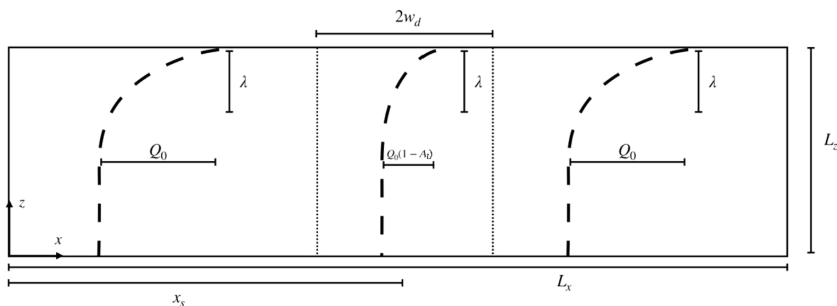


FIG. 1. Schematic of the system used for the simulations in this paper. The region between the vertical dotted lines, centered at x_s with width $2w_d$, is the shadowed region. The regions to the left and right of these dotted lines are referred to as the unshadowed regions. The dashed lines in each region denote the vertical shape of the solar forcing term in Eq. (1c) in each region. λ is fixed between regions, but the magnitude of the forcing at the surface is reduced by a factor of $(1 - A_l)$ in the shadowed region. See Tables I and II for parameter definitions.

The first z -dependent factor is the shape of the Beer-Lambert law and determines the vertical distribution of heat added to the system [21]. The second term determines horizontal distribution of heat. This particular form creates a region with incoming radiation damped by a factor of A_l centered at position x_s with width $2w_d$ as in Fig. 1. The sharpness of the boundary is determined by the exponent $8w_d$. The sharpness of the boundary is an important system parameter because the spectral nature of the model requires 5–10 grid points across the interface to fully resolve the shadow boundary. In practice, the high resolution of the simulations performed ensures this with no significant restriction on the results. The magnitude of Eq. (2) is Q_0/λ [see Eq. (1c)]. Q_0 is given in Table I. This value of Q_0 corresponds to solar radiation intensity of 300 W/m^2 and is on the same order of magnitude as measurements of downwelling solar radiation above ice-covered lakes [20,32]. For simplicity, we neglect any effects of angled solar radiation as is typical at high latitudes in the winter. Including the effects of angled solar radiation—and therefore an angled shadowed region—will be considered in future work. λ is discussed below.

For the remainder of this paper, we will refer to the region with reduced solar radiation as the shadowed region and anywhere else as the unshadowed regions. The system parameters which are unchanged throughout this paper are listed in Table I. In Sec. III three system parameters are varied

TABLE I. System parameters used in this paper which are unchanged between simulations. For parameters which are varied see Table II. Units are given where appropriate.

Parameter	Description	Value
L_x	Lake width	16.384 m
L_z	Lake depth	4.096 m
N_x	Horizontal grid points	8192
N_z	Vertical grid points	2048
x_s	Shadow center	$L_x/2$ m
ρ_0	Reference density	1000 kg m^{-3}
ν	Kinematic viscosity	$10^{-6} \text{ m}^2 \text{ s}^{-1}$
κ	Temperature diffusivity	$1.43 \times 10^{-7} \text{ m}^2 \text{ s}^{-1}$
κ_C	Tracer diffusivity	$1 \times 10^{-6} \text{ m}^2 \text{ s}^{-1}$
Q_0	Magnitude of solar forcing	$7.1667 \times 10^{-5} \text{ }^\circ\text{C m s}^{-1}$
w_d	Shadow half-width	1 m

TABLE II. Table of cases. For unchanged parameters between cases see Table I. When referring to one of these cases in the text the case name in this table will be used. All values are exact except α , which is rounded to one decimal place.

Case name	T_0 (°C)	A_l	λ (m)	α (10^{-5}°C^{-1})
T02	2.5	0.9	0.4	2.2
T0B	2.5	0	0.4	2.2
Al6	2.5	0.6	0.4	2.2
Al3	2.5	0.3	0.4	2.2
T01	1.5	0.9	0.4	3.6
T03	3.5	0.9	0.4	0.8
La2	2.5	0.9	0.2	2.2
La8	2.5	0.9	0.8	2.2

to probe the effect these parameters have on the resulting motion. All cases used in this paper are presented in Table II. The parameters we vary are (1) T_0 , the initial temperature, (2) A_l , the albedo under the shadow, and (3) λ , the attenuation coefficient which determines the vertical structure of Eq. (2).

There are two main features of interest that interact with the developing motion: (1) the horizontal density difference at the shadow boundary (determined by A_l and the equations in Sec. II A) and (2) the vertical density gradient in the unshadowed region (determined by λ and Q_0). The vertical density gradient is immediately unstable because the initial temperature, T_0 , of the domain is below T_{MD} . The magnitude of the vertical gradient will grow until the fluid begins to overturn via RT instabilities. However, the horizontal density difference will generate motion from the outset of the simulations (the amplitude of the motion will be small for early times). Like the vertical density difference, the horizontal density differences will grow over time due to the consistent solar forcing.

1. Tracers

A passive tracer, C , obeys the following equation of motion:

$$\frac{DC}{Dt} = \kappa_C \nabla^2 C, \quad (3)$$

where the left-hand side says that the passive tracer follows the fluid flow and the right-hand side represents the effects of diffusion. The tracer represents a dye used in laboratory experiments to visualize the fluid motion. The tracer diffusivity, κ_C was chosen to match the kinematic viscosity, ν . The effects of diffusion are minimal inside the intrusion and do not play a large role in its development, therefore, it can be thought of as loosely representing any particulates, dissolved matter or organisms which may be suspended in the water column. C has no effect on the fluid density (hence the label “passive”) and has no source or sink terms. In the context of this process study, the main purpose is to visualize the developing flow due to the shadowing. The units of C are chosen to be a concentration, where a value of 1 indicates maximum saturation and a value of 0 to indicate that no tracer is present. At $t = 0$, two passive tracers are initialized which do not interact with each other, nor the fluid density. The first tracer, denoted as C_H , is arranged in a column at the center of the domain [Fig. 2(a)] with an initial width of $w_d = 2$ m, coinciding with the shadowed region. The column is assigned a concentration of 1, with sharp transitions on both sides to zero for the rest of the domain. We analyze this tracer using the vertical mean as a function of time. The vertical mean is defined as

$$\langle \cdot \rangle_z = \frac{1}{L_z} \int_0^{L_z} dz. \quad (4)$$

The purpose of $\langle C_H \rangle_z$ is to quantify the horizontal transport away from the center.

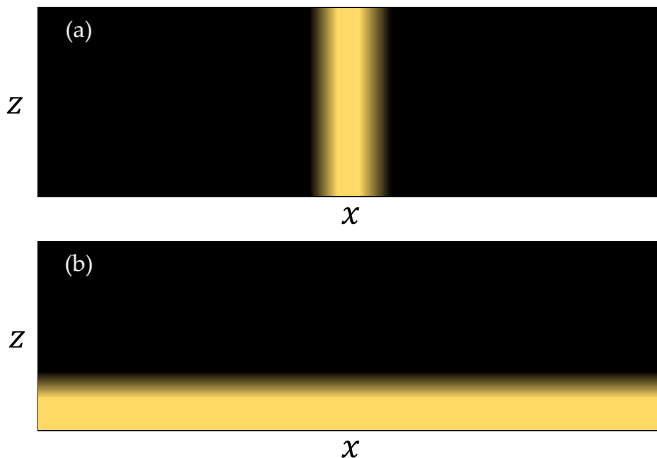


FIG. 2. Initial conditions of the two passive tracers are presented here. (a) Tracer C_H initialized as a column at the center of the domain with a maximum concentration of 1 at the center. (b) Tracer C_V initialized in a region 1 m in height at the bottom of the domain with a concentration of 1 at the bottom.

The second tracer, denoted as C_V , is initialized in a region of width 1 m at the bottom of the domain with a sharp transition from 1 to 0 at the top side [Fig. 2(b)]. This tracer is meant to quantify the vertical transport, and as such the evolution of the horizontal mean of C_V is of use. The horizontal means is defined as

$$\langle \cdot \rangle_x = \frac{1}{L_x} \int_0^{L_x} dx. \quad (5)$$

The purpose of $\langle C_V \rangle_x$ is to quantify the vertical transport up from the bottom.

2. Bulk motion

One approach to quantifying the bulk motion is to calculate the average kinetic energy per unit mass (KE_{avg}), which is an important quantity in the energy balance in ice-covered lakes [10]. Define KE_{avg} as

$$\text{KE}_{\text{avg}} = \frac{1}{2V} \int_V |\vec{u}|^2 dV. \quad (6)$$

KE_{avg} changes in time according to [10,33]

$$\frac{d\text{KE}_{\text{avg}}}{dt} = -\frac{g}{\rho_0 V} \int_V \rho w dV - \frac{1}{\rho_0 V} \int_V \phi dV. \quad (7)$$

The first term on the right-hand side is the average vertical buoyancy flux per unit mass, which we will denote as Φ_{avg} . The negative sign reflects a decrease in KE_{tot} when there is a net upwards buoyancy flux. The second term is the average viscous dissipation per unit mass, which we will denote as ϕ_{avg} . The negative sign reflecting that viscous dissipation always converts mechanical energy into heat. It is computed as $2\nu\rho_0 e_{ij}e_{ij}$, where e_{ij} is the rate of strain tensor, and is then integrated over the volume.

KE_{avg} gives information about motion in the system but provides no pointwise information about the motion. We can isolate the horizontal and vertical components of the velocity vector by partitioning KE_{avg} into KE_{avg_x} and KE_{avg_z} . We can enhance this partitioning further by calculating

the fraction of horizontal KE and the fraction of vertical KE, written as

$$\frac{\text{KE}_{\text{avg}_i}}{\text{KE}_{\text{avg}} + \delta}, \quad (8)$$

where i is x or z . δ is a small parameter to avoid dividing by zero in the initial condition where KE_{avg} is zero. An alternative to Eq. (8) is the ratio between the horizontal and vertical root-mean-squared velocities, called the Flow Geometry metric presented in Ref. [34]. While these related quantities are algebraically different, we found that they were sufficiently similar for purposes of our analysis.

3. Density differences at the shadow boundary

It is the horizontal density differences across the shadow boundary which dictate the emergence of lateral circulation in the system discussed in this paper. The initial sharpness of the shadow boundary is less important. The temperature changes due to the heating described by Eq. (2) are sufficiently small that we can use a linear equation of state in order to estimate an expression for the density difference across the shadow boundary

$$\rho(T) = \rho_0[1 + \alpha(T - T_0)]. \quad (9)$$

We can then write the background temperature difference between the region under the shadow and the region away from the shadow. Here α is the thermal expansion coefficient that is a function of T_0 only. T_0 is chosen to match the initial temperature in each of cases described in Table II. α is calculated as $\frac{1}{\rho_0} \frac{d\rho(T)}{dT} |_{T=T_0}$ for each case, using the same equation of state used in the simulations [30]. An approximate expression for α , which is quadratic in temperature, can be found in Ref. [13]. At early times, advection and diffusion terms in Eq. (1c) are small compared to the forcing term. The temperature field is thus determined by the forcing alone and reads

$$T_b = \frac{Q_0}{\lambda} F(x, z)t + T_0. \quad (10)$$

Using Eq. (9) and T_b , we can calculate the density difference between the density at the shadow center, x_s , and the density far from the shadow

$$\Delta\rho = \frac{\alpha\rho_0 Q_0 A_l F(z)}{\lambda} t, \quad (11)$$

where $F(z)$ is equal to the z -dependent part of $F(x, z)$ [Eq. (2)] alone.

T_0 , A_l , and λ are varied in this paper (Sec. III B) because they represent three different ways to alter the development of the lateral motion of interest. By varying T_0 , we change the local slope of the equation of state. Changing the local slope changes the development rate of RT instabilities and $\Delta\rho$ at the shadow boundary [Eq. (11)]. By varying A_l , the temperature difference across the shadow boundary is modulated, but the instabilities away from the shadow will develop at the same rate. By varying λ , this changes the vertical distribution of temperature, $F(z)$, and the density difference across the shadow boundary. Unlike T_0 and A_l , $\Delta\rho$ is inversely proportional to $1/\lambda$. The early time changes associated with horizontal density differences are captured by Eq. (11).

This quantity is used in Sec. III as a metric for understanding the development of motion as a result of the shadow. The time-independent coefficient of $\Delta\rho$ is plotted as a function of z for each of the cases in Fig. 3 (see Table II for list of cases). This shows how each of the relevant parameters change the vertical distribution of temperature across the shadow boundary. The coefficient of $\Delta\rho$ is linear in $\alpha(T_0)$ and A_l , hence the difference of $\Delta\rho$ in each case is just a shift in log-10 space for changes to T_0 and A_l . For La2 and La8, $\Delta\rho$ is inversely proportional to λ and so is the exponent of $F(z)$. As a result, the vertical structure and the magnitude at the surface are both modulated by changing λ .

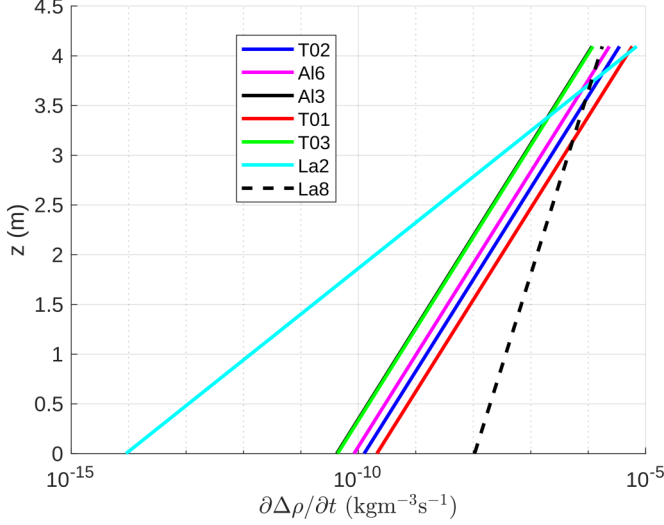


FIG. 3. The coefficient of $\Delta\rho$ [Eq. (11)] for each shadowed case (see Table II for full list). This coefficient is the rate of change of the density difference across the shadow boundary due to the background temperature alone.

C. Nondimensional parameters

Using the parameters listed in Tables I and II we use dimensional analysis (following [35], ignoring the shear flow aspects) to define a convective velocity scale U and temperature scale θ as

$$U = (g\alpha Q_0\lambda)^{1/3}, \quad (12a)$$

$$\theta = \left(\frac{Q_0^2}{g\alpha\lambda} \right)^{1/3}, \quad (12b)$$

using the linear equation of state, Eq. (9), unlike Ref. [35], which uses a quadratic fit. U is the velocity scale set by the density differences within the flow. We scale the temperature as $T = \theta\tilde{T} + T_0$, and θ is the scale of the temperature away from the initial temperature. In other words, T is nondimensionalized as $T = \theta\tilde{T} + \bar{T}$, where \bar{T} is the domain-averaged temperature [35,36]. The maximum temperature differences observed in each of the cases considered are $O(0.1^\circ\text{C})$, and therefore T_0 is a sufficient proxy for \bar{T} for our purposes. Using these scalings, assuming an advective timescale of λ/U , we can nondimensionalize the system and define the following set of dimensionless parameters:

$$\text{Gr} = \left(\frac{U\lambda}{\nu} \right)^2, \quad \text{Pr} = \frac{\nu}{\kappa}, \quad A_l, \quad \mu_1 = \frac{\lambda}{L_z}, \quad \mu_2 = \frac{w_d}{\lambda}, \quad \mu_3 = \frac{\lambda}{L_x}. \quad (13)$$

Gr is the Grashof number which is the relative strength of buoyancy and viscosity terms in the governing equations. Using Eq. (12a) it can be written as

$$\text{Gr} = \frac{(g\alpha Q_0)^{2/3} \lambda^{8/3}}{\nu^2}. \quad (14)$$

For the cases discussed in this paper Gr is $O(10^5)$ – $O(10^6)$. Variation of Gr is achieved through variations of α , which depends on the initial temperature, T_0 , in cases T01 and T03, and the attenuation length, λ , in cases La2 and La8.

Pr is the Prandtl number and defines the ratio of the momentum diffusivity to the temperature diffusivity. It is held constant at a value of 7 for all the cases considered in this study. This is a representative value for temperatures below T_{MD} and is used in studies of similar 2D nonhydrostatic simulations [14,15]. A Prandtl number of 10 has also been used in similar contexts [28,35].

A_l is the albedo and is nondimensional by definition. The remaining three parameters are the relevant nondimensional length scales for this problem. μ_1 is the nondimensional attenuation length. μ_1 has been studied in similar contexts to those studied here which showed experimentally that the magnitude of μ_1 determined the power-law relationship between the dimensionless vertical heat flux, the Nusselt number, and the Rayleigh number [36]. μ_2 is the ratio of the shadow width to the attenuation length and is the main aspect ratio of this system. μ_3 is the ratio of the domain width to the attenuation length. The attenuation length sets the horizontal scale of RT instabilities which are observed in this study. If μ_3 is too large, then full RT instabilities are unable to form, disrupting the primary dynamics explored in our simulations. In the cases considered in this study $\mu_3 < 0.05$.

Analytical models exist which predict some aspects of the evolution of horizontal flow due to lateral buoyancy differences [14,34]. Reference [34] studies lateral motion which emerges due to surface cooling and nonuniform bathymetry. The authors present a model which predicts three regimes (see Fig. 2 in Ref. [34]), the timescales of the transitions between regimes, and the velocity scales of the horizontal motion in each regime. Determining analytical expressions for the horizontal velocity and timescales in a similar fashion to Ref. [34] is an avenue for future work but is not the focus of the present study.

Two other options to define a velocity scale are a buoyancy velocity $u_b = \sqrt{g'\lambda}$ and a convective velocity $w^* = (B_* h_{CML})^{1/3}$. This form of u_b was used in a numerical study of radially spreading gravity currents as the horizontal velocity scale in a rotating and nonrotating tank [37] and is also the form of the shallow water wave speed [33]. $g' = g \frac{\rho_1 - \rho_0}{\rho_0}$ is the reduced gravity between two fluid layers, where ρ_1 is the denser fluid and ρ_0 is the less dense fluid. In our study, g' cannot be defined in terms of the initial conditions because the density is uniform everywhere. Instead we consider a representative temperature change of 0.3°C and use it to estimate u_b for the three initial temperatures considered in this paper (see Table II). With this assumption we find that $u_b \approx 1\text{--}10 \text{ mm s}^{-1}$, minimized for $T_0 = 3.5^\circ\text{C}$ and $\lambda = 0.2 \text{ m}$, and maximized for $T_0 = 1.5^\circ\text{C}$ and $\lambda = 0.8 \text{ m}$.

The typical vertical velocity scale within the CML is denoted by w^* , where h_{CML} is the depth of the CML [13,20,38]. w^* has also been linked to plankton settling rates using scaling arguments [39]. The simulations considered here do not have initial stratification, the primary balance against the deepening of the CML [11,14]. In addition, we do not consider sufficiently long timescales to allow a CML to form as in [14,15]. As such w^* is not directly applicable to our set up. Nonetheless, it is an important velocity scaling in the study of convection forced by solar radiation. Following the calculation of B_* , the effective buoyancy flux, in Ref. [13] we arrive at

$$w^* = [\alpha g Q_0 (\lambda e^{-h/\lambda} + h - \lambda)]^{1/3}.$$

There is no obvious choice for h_{CML} because there is no CML in our simulations. However, taking λ as h_{CML} we find

$$w^* = e^{-1/3} U \approx 0.72 U, \quad (15)$$

where U is the velocity scale in Eq. (12a). The velocity scales in a CML whose depth is comparable to the attenuation length is similar in magnitude to U . In Ref. [14] the smallest CML depth shown was $\approx 2 \text{ m}$ and later expanded to $\approx 10 \text{ m}$. In the limit of $h \gg \lambda$, a more realistic relationship, we find

$$w^* = (\alpha g Q_0 h)^{1/3} = \left(\frac{h}{\lambda}\right)^{1/3} U.$$

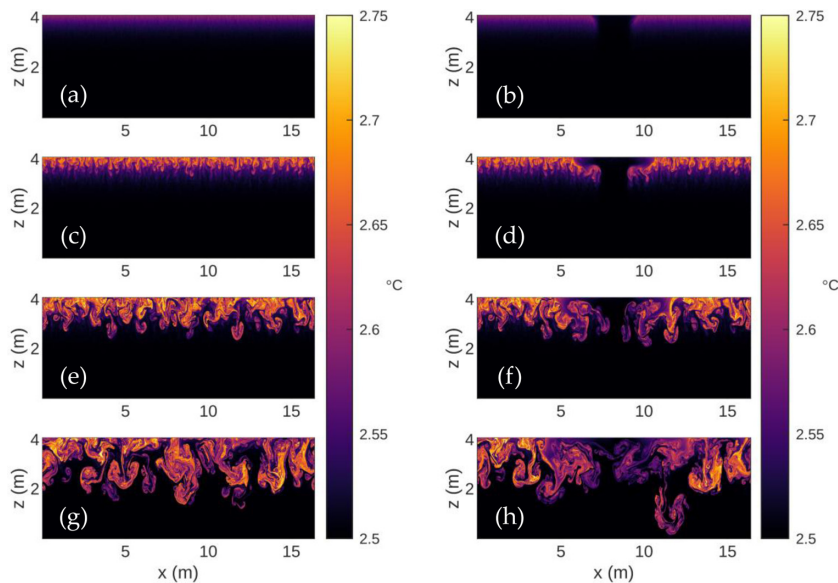


FIG. 4. Snapshots of the temperature field for T0B (a), (c), (e), (g) and T02 (b), (d), (f), (h) at (a), (b) 600 s, (c), (d) 1200 s, (e), (f) 1800 s, (g), (h) 2400 s. Both simulations use $T_0 = 2.5$ °C, $\lambda = 0.4$ m. T02 uses $w_d = 1$ m and $A_l = 0.9$. T0B is entirely determined by the development of RT instabilities. T02 additionally has the shadowed region to generate systematic lateral motion.

III. RESULTS

We find that a shadowed region inevitably (as depicted in Fig. 1) generates systematic lateral motion. This motion takes the form of a pair of lateral intrusions which flow outward away from the shadow near the surface and a return flow underneath. The return flow is strongest immediately below the intrusions and rapidly decays towards the bottom. The shadowed region also leads to earlier and enhanced vertical transport, compared to Rayleigh-Taylor (RT) instabilities alone. After describing an illustrative base case in Sec. III A, in Sec. III B T_0 , A_l , and λ are systemically varied, and in doing so we identify a qualitative relationship between the front position of the intrusion and each of these parameters. In all of these cases, noise is added to the initial temperature field in order to facilitate the growth of instabilities away from the shadowed region. In Sec. III C noise is removed from and compared with the illustrative base case from Sec. III A to quantify the effect of noise, and the resulting instabilities on the lateral motion.

To quantify the effect of the shadow, we employ case T02, or shadowed case with $T_0 = 2.5$ °C, $A_l = 0.9$, and $\lambda = 0.4$ m. T02 is compared with T0B, the unshadowed case with $T_0 = 2.5$ °C, $A_l = 0$, and $\lambda = 0.4$ m (see Table II). The set of parameters chosen for T02 and T0B represent specific regions of their respective parameter space. In particular, $T_0 = 2.5$ °C is near the midpoint between the freezing temperature and T_{MD} . $A_l = 0.9$ is representative of high albedo and, therefore, the largest density difference across the shadow boundary and high potential for lateral motion. $\lambda = 0.4$ m is chosen to represent a lake of moderate clarity as in Refs. [14,22].

A. Main comparison: Shadowed versus unshadowed dynamics

The development of the temperature fields in T02 and T0B are compared in the two columns of Fig. 4, T0B in the left column and T02 in the right column. Given the local linearity of the equation of state, the temperature is an adequate proxy for density. In T0B [Figs. 4(a), 4(c), 4(e), 4(g)] motion is generated exclusively via the development of RT instabilities. As the system is continually heated, the RT instabilities grow in both the vertical and horizontal. There are no signs

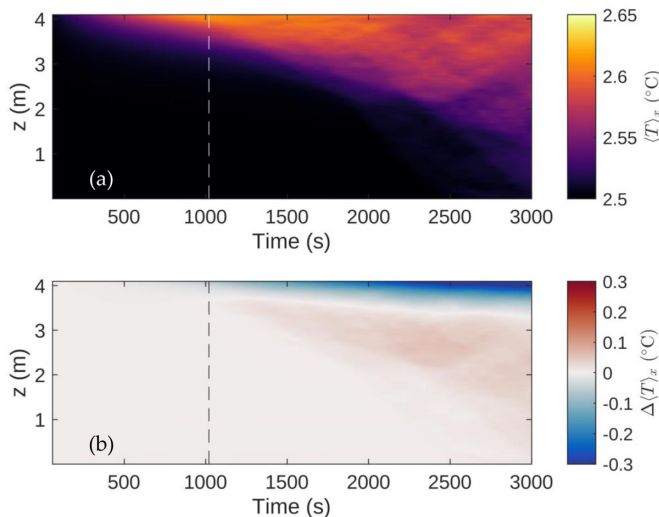


FIG. 5. (a) Evolution of the horizontally averaged temperature field for TOB. Vertical dashed line is superimposed to indicate the approximate transition time between a solar-radiation-dominated phase and a convective-dominated phase (defined in the text). (b) Deviation of the horizontally averaged temperature field from the background T_b [Eq. (10)]. The solid black line retains the same meaning as in panel (a). Positive values indicate that the horizontally averaged temperature is warmer than just the background, negative values are colder than the background.

of lateral motion on scales greater than the horizontal length scales of the RT instabilities. As mentioned in Sec. I, we refer to the region of space between the surface and the mean RT instability depth as the convective layer (CL). The spatial scales of the instabilities are set by the magnitude of the vertical density gradient away from the shadow. At early times, the temperature gradient closely resembles T_b , Eq. (10). The parameters which control this gradient are λ , α , and κ . In Sec. III B, λ and α are varied, the latter through the variation of T_0 . Reference [35] used linear theory to show that increasing λ decreased the growth rate of instabilities while increasing the dominant length scale. Increasing the T_0 decreases the magnitude of the vertical density gradient at fixed time and, therefore, decreases the growth rate of instabilities. However, the dominant length scale does not appreciably change with T_0 .

The CL develops through two distinct phases: (1) a solar-radiation-dominated phase where the mean temperature deviates only from T_b [Eq. (10)] by small amounts [Figs. 4(a) and 4(c)] and (2) a convection-dominated phase where RT instabilities transport temperature deeper into the water column and as a result, decreases the mean temperature near the surface, overcoming the constant heating [Figs. 4(e) and 4(g)]. These phases are shown to exist in Fig. 5. Left of the dashed line is the solar-radiation-dominated phase, characterized by a monotonically decreasing mean temperature profile in Fig. 5(a) and a deviation from the background temperature [Eq. (10)] of near zero in Fig. 5(b). Right of the dashed line is the convection-dominated phase, characterized by a nonmonotonic mean temperature profile driven by RT instabilities transporting heat deeper into the water column. Figure 5(b) shows the regions in which convection has cooled or heated the mean profile. The depth of the CL is defined in Fig. 5(a) as the maximum depth of fluid warmer than T_0 to the right of the dashed line. The CL is also visible in Fig. 5(b) as the maximum depth of the region adjacent to the surface which is warmer than the background.

The shadowed region in T02, in contrast, creates systematic horizontal density gradients that are larger than those associated with individual RT instabilities in the CL [Figs. 4(a) and 4(b)]. As a result, lateral intrusions emerge, advecting RT instabilities near the shadow boundary, down and inwards [by Fig. 4(d)] and upwards [by Figs. 4(f) and 4(h)]. The upwards motion of the return flow is

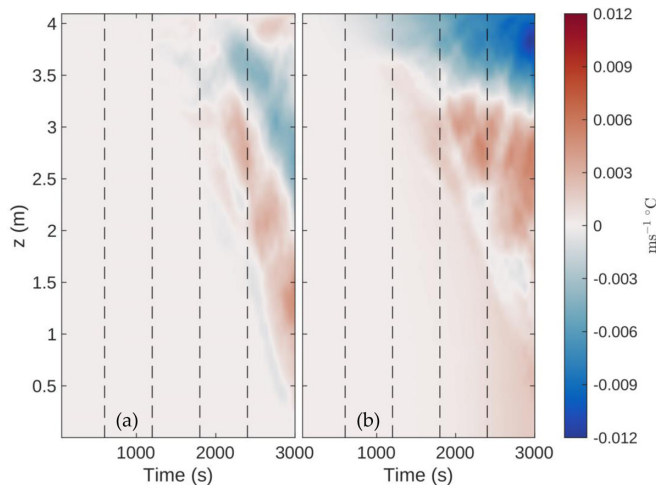


FIG. 6. Horizontally averaged, horizontal temperature flux where $T_0 = 2.5^\circ\text{C}$ for (a) TOB (unshadowed) and (b) T02 (shadowed). T02 in panel (b) is averaged over the left half of the horizontal domain to avoid cancellation of the lateral intrusion [see Figs. 4(d) and 4(f) for signs of symmetry which would cancel in an average]. Vertical dashed lines refer to the times corresponding to each row of Fig. 4, in order of increasing value.

evidence of an upwelling under the shadow from the intrusions that arises due to mass conservation as the intrusions propagate outward. The upwelling is found at the center of the domain, under the shadow, and is discussed further in Sec. III A 1. As time progresses, the intrusions continue to flow outwards, disrupting the CL near the surface. The return flow acts as a mechanism for distributing heat under the shadow but is unsurprisingly insufficient to overcome the damped heating in the shadowed region.

The intrusions themselves are similar to a classical gravity current. A tall current head with a narrow body propagating from a low density region to a higher density region [Fig. 4(d)]. However, there are some ways in which this diverges from classic gravity currents. The ambient is changing gradually with time and RT instabilities are transporting heat downwards and cool fluid upwards. After some time has passed, the intrusions are not always propagating into denser fluid, but instead propagating into an oscillating temperature field about the mean value shown in Fig. 5(a). This oscillation is apparent in Fig. 4(h) and somewhat in Fig. 4(f), where cool plumes reach the surface and, hence, the density difference at the front of the intrusions is oscillating, rather than constant. In Sec. III C we identify that these changes at the front of the intrusion due to the growth of RT instabilities indeed have a small effect on the propagation speed of the intrusions.

1. Mean temperature flux

The development of the temperature field in Fig. 4 demonstrates the effect of the shadowed region on the motion of the intrusions and the return flow immediately below the intrusion. The motion of the fluid under the shadow and closer to the bottom proceed due to the incompressibility assumption, however, due to the small temperature gradients at the bottom and under the shadow this motion doesn't manifest in the temperature field. Visualization of these features are quantified using the horizontally averaged, horizontal temperature flux, $\langle uT \rangle_x$, and the vertically averaged, vertical temperature flux, $\langle wT \rangle_z$ [where these averages are defined in Eqs. (5) and (4), respectively]. $\langle uT \rangle_x$ is averaged over the left half of the domain to avoid averaging out the motion of the intrusions.

In TOB, the unshadowed case, in Fig. 6(a) mean horizontal fluxes develop in the CL [Figs. 4(e) and 4(g)] and follow its descent to the bottom of the domain at later times. While there are nonzero mean fluxes in this system, there are no mechanisms for transport at depths below the CL or beyond

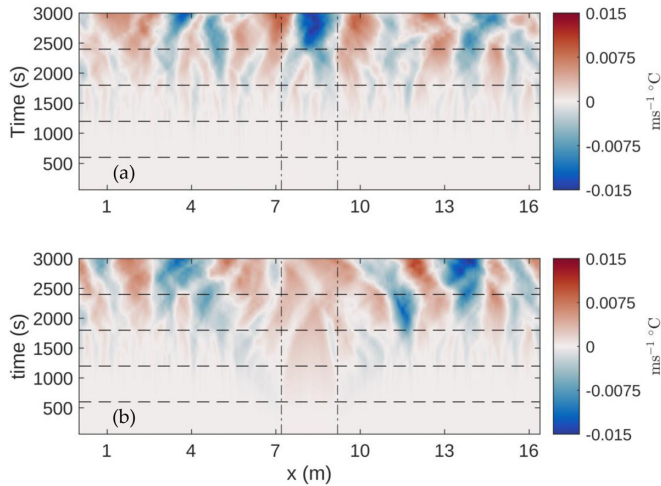


FIG. 7. Vertically averaged, vertical temperature flux where $T_0 = 2.5^\circ\text{C}$ for (a) TOB (unshadowed) and (b) T02 (shadowed). Vertical dashed lines indicate the edge of the shadowed region. Vertical dot-dashed lines refer to the approximate edge of the shadow boundary. Horizontal dashed lines refer to the times corresponding to each row of Fig. 4, in order of increasing value.

the horizontal length scales of the RT instabilities, as shown in Fig. 6(a). In addition, the mean fluxes at fixed depth are nonmonotonic in time, suggesting a lack of systematic motion due to the random orientations of the convective plumes.

This is in contrast to the shadowed case, T02, where the fluxes near the shadow boundary dominate $\langle uT \rangle_x$ [Fig. 6(b)]. At all times, there is a large, increasing mean flux away from the center ($\langle uT \rangle_x < 0$) at the surface, driven by the intrusion. Below this region is a mean temperature flux towards the center ($\langle uT \rangle_x > 0$) that extends to the bottom of the domain. After 2000 s the return flow dominates the mean at depths below the intrusions, even as the CL continues to develop. This is confirmed by comparing $\langle uT \rangle_x$ inside the CL for both Figs. 6(a) and 6(b).

The fluxes near the bottom in the return flow are smaller in magnitude than those in the intrusions and the return flow immediately below the intrusion, but are systematic in a manner which does not appear in TOB [Fig. 6(a)]. The strength of these fluxes naturally will depend on the size of the domain, especially for shallow systems.

The depth of the boundary between motion toward and away from the center in Fig. 6(b) moves downwards in time, at a rate slower than the descent of the CL. This suggests that the region effected by the intrusion also expands in the vertical in time. The ordered nature of $\langle uT \rangle_x$ in the shadowed case persists for the entirety of the time frame considered. Both the shadow and unshadowed case produce fluxes on the same order of magnitude, but in the shadowed case it is systematically stronger, more ordered, dominates more quickly, and affects the entire vertical domain before the descent of the CL.

The vertically averaged, vertical temperature flux in TOB [Fig. 7(a)] evolves similarly to the CL. When the fluxes are small, appearing as thin streaks, as they are at early times in Fig. 7(a) or in Fig. 7(b)—away from the shadow—then the CL has yet to form and descend in the water column. When the fluxes are large—and irregular—at later times it is due to the presence of large convective cells that extend from the top to the bottom of the domain and interact with the top and bottom boundary at the latest times.

The shadow has the effect of introducing larger and more coherent fluxes near and under the shadow at early times as seen at the bottom half of Fig. 7(b). These fluxes are small compared to the fluxes at late times, but are relatively large compared to the fluxes away from the shadow at the same time. There is also a persistent effect of upwelling at late times on a larger scale than the

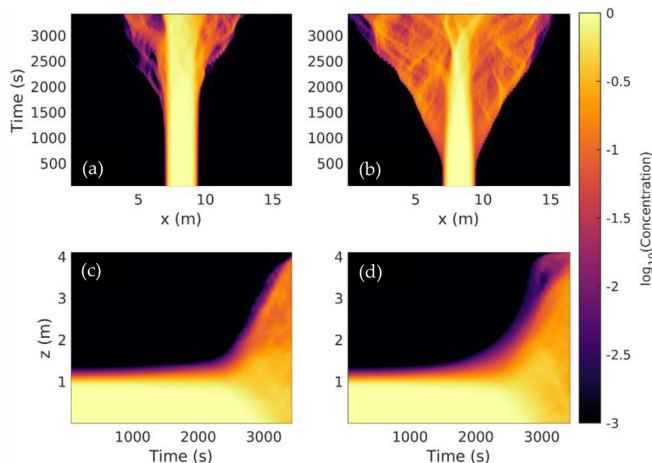


FIG. 8. The horizontal and vertical mean of passive tracers highlighting enhanced transport due to the lateral motion generated by the shadowed region. Initial conditions given in Fig. 2. (a), (b) Tracer arranged in a column centered at the center of the domain with width $2w_d$. Unshadowed case in panel (a) and shadowed case in panel (b). (c), (d) Tracer aligned in a row at the bottom of the domain with a width of 1 m. Unshadowed case in panel (c) and shadowed case in panel (d).

RT instabilities at those times. At early times, the region under the shadow shows a smooth, mean upward flux, free of any irregular features. This net vertical motion under the shadow is responsible for the motion towards the surface of the return flow immediately beneath the intrusion in Figs. 4(d) and 4(f). On the boundary of the shadowed region is a mean downwelling of warmer fluid, showing signs of the RT instabilities which are pushed downwards in response to the horizontal expansion of the intrusions.

In the unshadowed case at later times, the patches of positive and negative fluxes in Fig. 7(a) reveal the approximate horizontal length scales of the plumes at this stage. These are the opposing fluxes driven by the cool and warm plumes which propagate past each other, visible in Figs. 4(e) and 4(g). Contrasting this to Fig. 7(b), the region near the shadow is dominated by patches of positive (upward) fluxes, indicating that as the intrusion propagates outwards, the region of upwelling—initially confined to the shadow boundary—expands as well. $\langle wT \rangle_z$ in the shadowed case shows that a shadow enables vertical transport at an earlier time than the unshadowed case, which is driven by RT instabilities alone. Both Figs. 6(b) and 7(b) show the potential for significant transport due to the shadow over length scales exceeding the RT length scales and over timescales faster than the RT development timescale.

2. Vertical and horizontal tracer transport

The quantification of vertical and horizontal tracer transport is carried out using the two independent, passive tracers $\langle C_H \rangle_z$ and $\langle C_V \rangle_x$, respectively, with initial conditions as discussed in Sec. II B 1 and averages defined in Eqs. (4) and (5). In Sec. III A 1 the locations of significant horizontal [Fig. 6(b)] or vertical [Fig. 7(b)] transport of temperature is quantified. Using $\langle C_H \rangle_z$ and $\langle C_V \rangle_x$, the amount of tracer transported and the distance of maximum transport over time can be quantified. The development of tracer $\langle C_H \rangle_z$ for shadowed and unshadowed cases are shown in Figs. 8(a) and 8(b). The development of tracer $\langle C_V \rangle_x$ for shadowed and unshadowed cases are shown in Figs. 8(c) and 8(d).

Despite the existence of horizontal temperature fluxes with similar magnitude in the unshadowed case [Fig. 6(a)] and shadowed case [Fig. 6(b)], the tracer C_H is transported further from the center in the shadowed case, with transport beginning earlier in time. Even at later times, when the mean fluxes have comparable magnitudes, the transport in the unshadowed case is unremarkable.

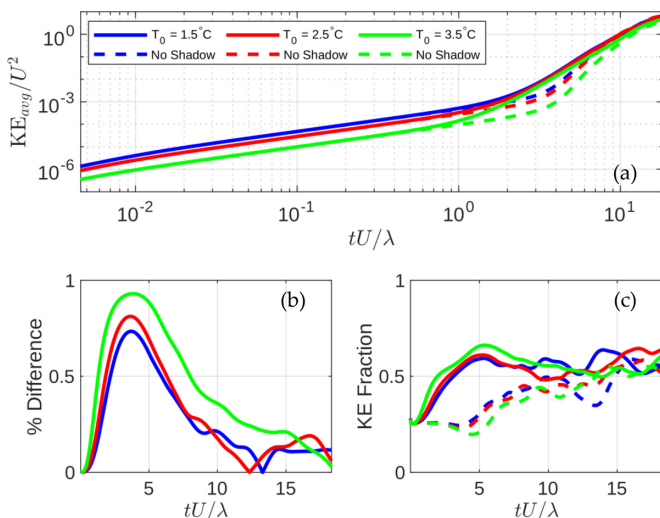


FIG. 9. (a) Average kinetic energy per unit mass as a function of time for the three values of T_0 1.5, 2.5, and 3.5°C . The average kinetic energy per unit mass is given for both the shadowed (solid) and unshadowed (dashed) case, for each T_0 . Horizontal and vertical axes on logarithmic scales. (b) Percent difference between the shadowed and unshadowed KE_{avg} . (c) Fraction of horizontal KE in the shadowed (solid) and unshadowed (dashed) cases. All axes in each panel are dimensionless.

In the unshadowed case, averaging in the vertical eliminates most lateral transport in the first 1500 s. Significant net horizontal transport is only achieved when upwelling cool plumes or downwelling warm plumes reach the bottom or top boundary. In the shadowed case, the density difference is largest at the upper boundary (see Fig. 3) and is immediately converted into lateral motion. C_H is transported earlier, farther away, and the maximum transported distance at each time is constantly increasing. At the latest times shown, any remnants of the initial conditions are almost completely destroyed by the horizontal fluxes in the shadowed case [Fig. 8(b)], while the initial structure remains in the unshadowed case [Fig. 8(a)].

The vertical transport from the bottom is not as significantly modified as the lateral transport [comparing Fig. 8(c) to Fig. 8(d)]. However, there are some minor differences that can be identified: (1) the transition from smooth $\langle C_V \rangle_x$ to well mixed at later times happens sooner in the shadowed case, but more gradually (2) $\langle C_V \rangle_x$ reaches the surface at an earlier time in the shadowed case.

3. Bulk motion

Figure 9 presents the average KE per unit mass for cases T01, T02, and T03 (see Table II) and is nondimensionalized using the scalings presented in Sec. II C. The evolution of the average KE per unit mass [Fig. 9(a)] on a logarithmic scale behaves as two linear regimes, with an initially shallow slope and a transition to a steeper slope at later times. The presence of the shadow does not effect the slope of either the pre- or posttransition curves. Instead, the shadowed cases transition earlier in time.

The time axes are labeled as tU/λ , where t is physical time (measured in seconds) and U/λ is the inverse of the advective timescale. The vertical axis in Fig. 9(a) is labeled as KE_{avg}/U^2 where $1/U^2$ is the inverse scaling of energy per unit mass. The vertical axes in Figs. 9(b) and 9(c) are nondimensional by definition. The key parameter in the comparison presented in Fig. 9 is α , where $\lambda/U \propto \alpha^{-1/3}$ and $U^2 \propto \alpha^{2/3}$. This suggests that an increase to T_0 , which decreases α , increases the timescale and decreases the KE scale, with a stronger dependence on the KE scale. In Fig. 9(a) the curves are initially separated by a vertical shift but collapse in both the shadowed and unshadowed cases after the transition, suggesting that a separate velocity scale is required for the

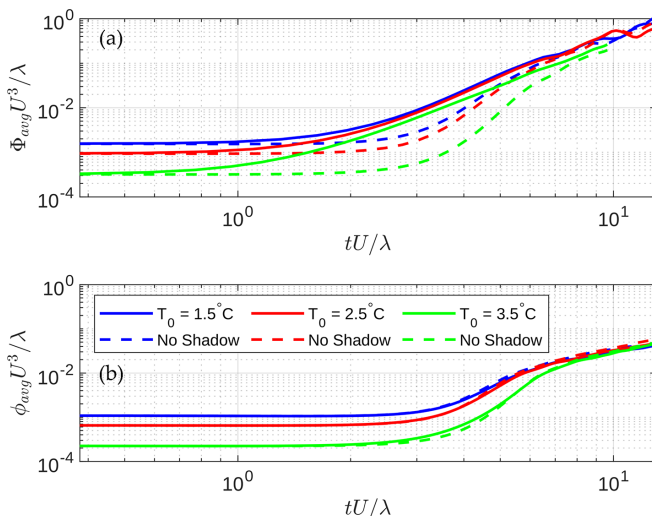


FIG. 10. The rate of change of the average kinetic energy per unit mass with respect to time is a function of (a) the average buoyancy flux per unit mass, Φ_{avg} and (b) the average dissipation per unit mass, ϕ_{avg} . In both panels the quantity for both the shadowed and unshadowed equivalent are given. The legend in panel (b) also applies to panel (a). All axes in both panels are dimensionless.

early time evolution. In terms of dimensional variables, cases with different T_0 never collapse. This is also captured in the percentage difference between the shadowed and unshadowed KE shown in Fig. 9(b). The horizontal offset in Fig. 9(b) for $tU/\lambda < 5$ shows clearly that a different velocity scale exists during the growth of the lateral intrusions prior to the convection-dominated phase.

The transition in the shadowed cases appears to begin at $tU/\lambda \approx 1$ where the KE_{avg} curves visibly diverge from their unshadowed counterparts with timing independent of T_0 . The percent difference between KE_{avg} for the shadowed and unshadowed cases, for each T_0 , reveals that this diverging behavior—or enhancement of KE_{avg} —in the shadowed case is growing from the onset of the simulation [Fig. 9(b)]. In physical time, the initial growth in the percentage difference collapses for all three cases suggesting that the growth rate in this phase is independent of T_0 [Fig. 9(b)]. The vertical offset is unchanged in terms of physical variables.

The transition in the unshadowed cases, however, is a function of T_0 and, therefore, α . The transition is the characteristic elbow of KE_{avg} , which is significantly sharper than in the shadowed cases [Fig. 9(a)]. It is also seen in the percentage difference between each pair of shadowed and unshadowed cases [Fig. 9(b)], where the percent difference reaches its maximum for each T_0 . In dimensionless time, as shown here, the transition time collapses to $tU/\lambda \approx 4$. In physical time, the transition time for the unshadowed cases is an increasing function of T_0 , caused by the nonlinearity of the equation of state.

The rate of change of KE_{avg} is determined by the average buoyancy flux per unit mass, Φ_{avg} , and the average dissipation per unit mass, ϕ_{avg} [Eq. (7)]. These quantities are presented in Fig. 10 as dimensionless variables. ϕ_{avg} is comparable between shadowed and unshadowed cases [Fig. 10(b)], in contrast to Φ_{avg} [Fig. 10(a)], and so naturally the enhanced buoyancy flux dominates these results.

Comparing the times of the change in slope between Figs. 9(a) and 10(a) for each T_0 case, it is clear that the change in KE_{avg} , between the shadowed and unshadowed cases is driven entirely by the enhanced buoyancy flux generated by the shadowed region. Φ_{avg} is inevitably equalized at long times, resulting in a convergence of KE_{avg} between shadowed and unshadowed cases. As with Fig. 9(a), the scalings from Sec. II C are insufficient to correct the initial differences in Φ_{avg} at early times, but the curves collapse after the transition, further cementing that a different set of scalings is required for the early time behavior.

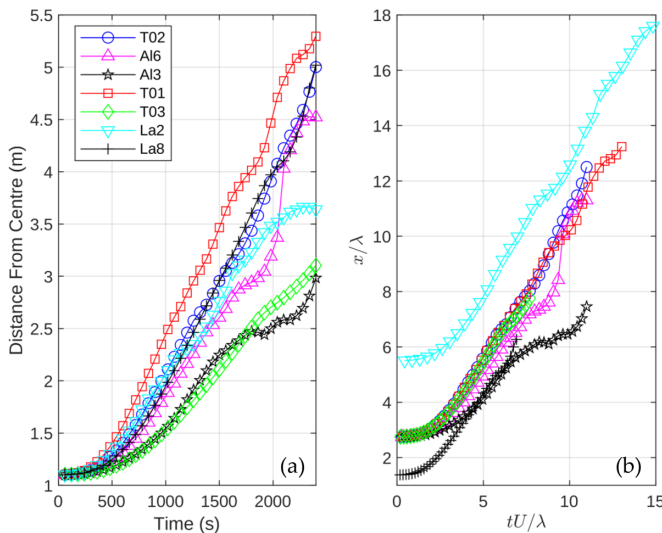


FIG. 11. Position of intrusion front as a function of time at 60 s intervals for each case listed in Table II in both (a) dimensional and (b) dimensionless variables. The front position is tracked using the tracer C_H defined in Sec. II B 1 with initial conditions defined in Fig. 2(a). There is the main system T02, presented in Sec. III A, and two variations from this system for each parameter varied in Sec. III B: T_0 , A_l , and λ .

While Φ_{avg} is a quantity calculated from the product of the vertical velocity and the density [Eq. (7)], it is enabled in this system by the capacity to generate horizontal motion. This is captured in the ratio of the average KE per unit mass in the horizontal ($\text{KE}_{\text{avg}_x} = 1/V \int_V u^2/2 dV$) to the average KE per unit mass [Eq. (8)]. This ratio is given in Fig. 9(c). The large increase in Φ_{avg} in Fig. 10(a) in both the shadowed and unshadowed cases is correlated with an increase in the fraction of KE in the horizontal [Fig. 9(c)]. When the shadowed cases complete their transitions in KE_{avg_x} , $\text{KE}_{\text{avg}_x}/\text{KE}_{\text{avg}}$ is near 0.5. Similarly in the unshadowed cases, the transition is completed once KE_{avg_x} and KE_{avg_z} are comparable [Fig. 9(c)]. The unshadowed case catches up in terms of KE_{avg} and the buoyancy flux. This may occur because of the finite vertical domain but is not explored in this research.

B. Parameter variations

In the following sections, the parameters T_0 , A_l , and λ are systematically varied to assess how they effect the lateral circulation and transport identified in Sec. III A. Justification for varying these parameters is given in Sec. II B 3. Figure 11(a) shows the front position as a function of time associated with each simulation, to be discussed further for each parameter. Figure 11(b) gives the nondimensionalized front position, x/λ , as a function of the nondimensional time, tU/λ . In Fig. 11(a) we see an initial acceleration phase followed by a period with nearly constant speed. Nondimensionalizing shows that apart from changes in albedo (cases Al3 and Al6) the speed of the intrusion collapses. Cases La2 and La8 are shifted vertically due to the change in λ .

In each section a common figure layout with six panels and two columns is used: Fig. 12 for the T_0 variation, Fig. 14 for the A_l variation, and Fig. 16 for the λ variation. The left column panels [(a), (c), and (e)] are the mean temperature to a depth of λ below the surface. The right column panels [(b), (d), and (f)] are snapshots of the temperature field at a time indicated by the horizontal, dashed line in the left column.

The left column has three important pieces of information encoded in it: (1) the large characteristic V shape shows the horizontal extent (width) and speed (slope) of the intrusion as a function of time, (2) the solar-radiation-dominated phase is characterized by long, vertical streaks in the mean temperature field, and (3) the convection-dominated phase, which immediately follows the

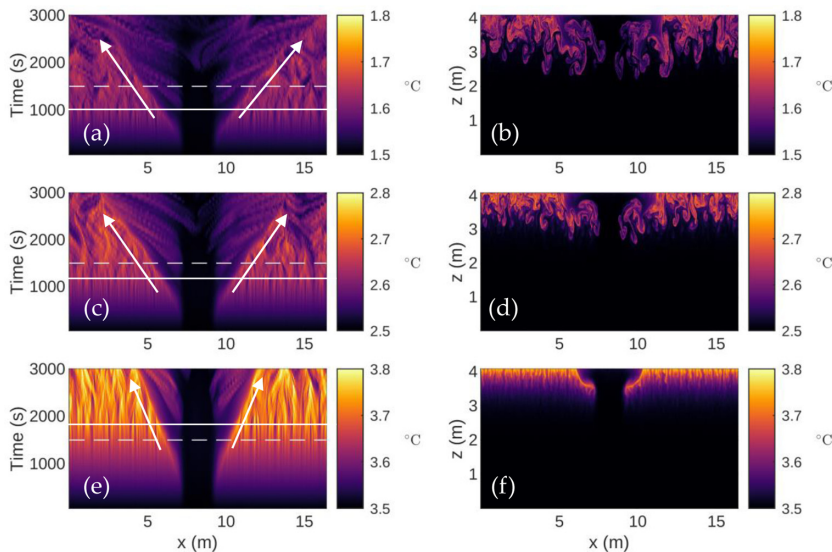


FIG. 12. Averaged and full temperature fields for T01, T02, and T03. (a), (c), (e) Vertically averaged temperature field vs time. Vertical average evaluated from $z = L_z \rightarrow L_z - \lambda$. (b), (d), (f) Snapshots of the full temperature field at $t = 1500$ s for each value of T_0 . Corresponds to the horizontal dashed line in (a), (c), (e). (a), (b) $T_0 = 1.5^\circ\text{C}$, (c), (d) $T_0 = 2.5^\circ\text{C}$, (e), (f) $T_0 = 3.5^\circ\text{C}$. Solid horizontal line indicates the approximate transition time between the solar-radiation-dominated phase and the convection-dominated phase of RT instability development. Solid arrows are a guide to the eye which indicate the bounds of the character V shape discussed further in the text.

solar-radiation-dominated phase, is characterized by branching of these streaks. The approximate transition time between the two phases is give by the solid white line. The purpose of the right column is to compare the progression of the intrusions in the full temperature field at fixed time.

There are two apparent phases to the front position: (1) the acceleration phase, where the slope of the front position is increasing and (2) the propagation phase, characterized by a nearly constant propagation speed. These front positions are estimated from the tracer C_H , defined in Sec. II B 1. The front position at later times are subjected to large plumes near the surface, which means the front position is less coherent and harder to identify algorithmically at later times, but it often still easy to identify directly.

1. Initial temperature

In this paper, the initial temperature is fixed to some $T_0 < T_{MD}$. In the main system, denoted as T02, $T_0 = 2.5^\circ\text{C}$ and in this section (and Sec. II B 2) we also consider $T_0 = 1.5, 3.5^\circ\text{C}$, or cases T01 and T03.

The slope of the equation of state approaches zero as $T_0 \rightarrow T_{MD}$ (top to bottom in Fig. 12), and therefore larger changes in temperature are required to obtain similar $\Delta\rho$. As a result, the solar-radiation-dominated phase is prolonged (solid horizontal line in left column of Fig. 12). The intrusion propagates approximately 2 m (indicated by the width of the V shape) by the end of the solar-radiation-dominated phase, with only minor variations between each T_0 case.

In the convection-dominated phase, we observed a near-constant front speed of the intrusion as indicated by the characteristic V shape at the center of Figs. 12(a), 12(c), and 12(e). The V is widest over the time period of interest when $T_0 = 1.5^\circ\text{C}$ in Fig. 12(a). The width of V shrinks with increasing T_0 in Figs. 12(c) and 12(e). The change in width of the V is not constant with T_0 and has a more extreme change between Figs. 12(c) and 12(e), due to the nonlinearity of the equation of state. The full temperature fields [Figs. 12(b), 12(d), and 12(f)] indicate the same trends.

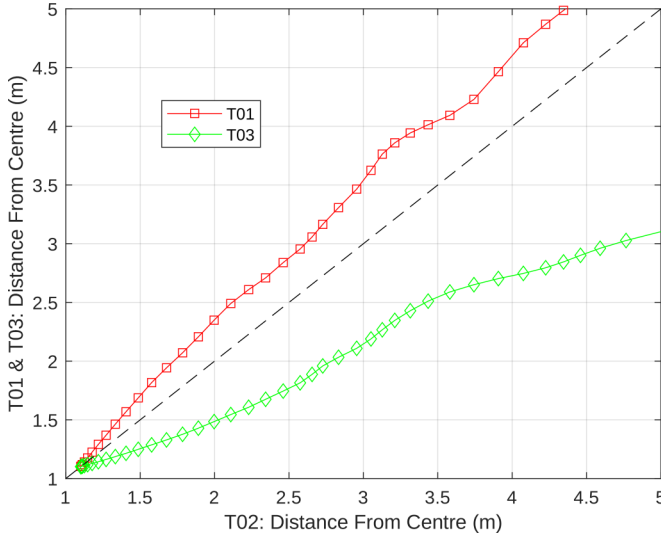


FIG. 13. Intrusion front positions of T01 and T03 as a function of the intrusion front position for the main shadowed system (T02). Symbols are front positions extrapolated from SPINS output separated by a time interval of 60 s, connecting lines are a guide to the eye. If a curve is above the diagonal, dashed line, then it has propagated further than T02 up to that time. If it is below the diagonal line T02 has propagated further over the same time interval. Curves parallel to the diagonal are propagating at the same speed.

T01 and T02 are at similar stages of development of the RT instabilities and the intrusion, although T01 is more mature. The features in T03 are significantly less mature and the case is still in the solar-radiation-dominated phase at the time chosen.

Figure 13 compares the front position of the intrusion in T01 and T03 as a function of the front position in T02 (the base case). Over the first 2–2.5 m, the separation between the T01 and T03 front positions and the T02 front position is increasing linearly, showcasing the differences in the growth rate of the intrusions in the acceleration phase. Following this initial separation in intrusion front position, T01 and T02 propagate at very similar rates (showcased by how the T01 curve is parallel to the diagonal). The T03 case propagates at a similar rate for a short duration (approximately 1 m) before slowing dramatically. At this stage of the simulation, temperatures near the surface are approaching T_{MD} and are likely causing the intrusion to rapidly slow.

As T_0 is moved further from T_{MD} (i.e., closer to 0), the duration of the solar-radiation-dominated phase is shortened. This speeds up the development of the intrusion, but does not significantly effect the distance traveled over the solar-radiation-dominated phase. In all three cases, over the time considered, the intrusion continues to propagate until the end of the simulation.

2. Albedo

In the following analysis we consider two smaller values of A_l in addition to $A_l = 0.9$ (T02) from the base case. The small values are 0.6 (A16) and 0.3 (A13). Unlike T_0 , changing A_l only changes the density gradients at the shadow boundary and has no effect on the growth rate of RT instabilities. Similarly to changing T_0 , varying A_l only results in a shift in $\Delta\rho$ (Fig. 3), and with the right values can result in a very similar $\Delta\rho$. In addition to comparing the cases with varying A_l , we can also compare the A13 case to the T03 case, where $\Delta\rho$ is effectively equal.

By systematically varying A_l , we can better isolate the lateral motion. Figures 14(a), 14(c), and 14(e) gives the mean temperature field near the surface for decreasing A_l from Figs. 14(a) to 14(c) to 14(e). There are two main consequences of decreasing A_l : (1) the width of the characteristic V shape in Figs. 14(a), 14(c), and 14(e) decreases; and (2) the temperatures inside the V are larger.

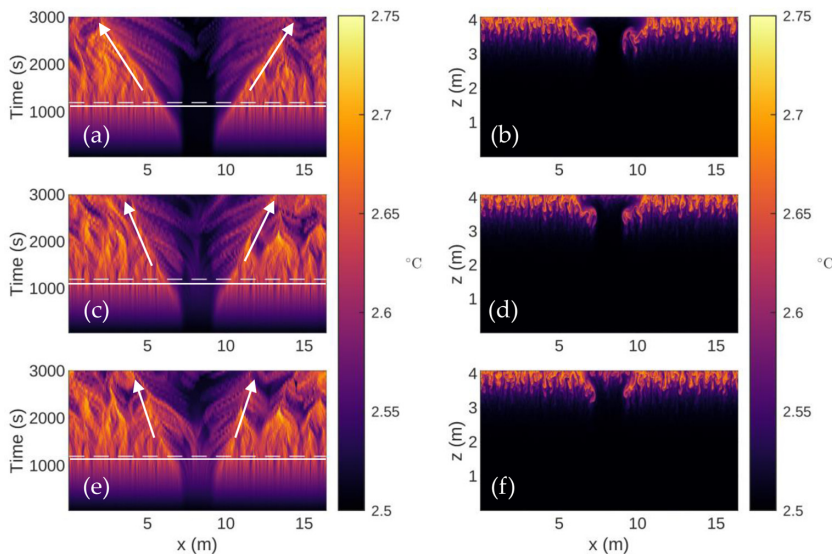


FIG. 14. Averaged and full temperature fields for T02, A16 and A13 (a), (c), (e) Vertically averaged temperature field vs time. Vertical average evaluated from $z = L_z \rightarrow L_z - \lambda$. (b), (d), (f) Snapshots of the full temperature field at $t = 1500$ s for each value of T_0 . Corresponds to the horizontal dashed line in (a), (c), (e). (a), (b) $A_l = 0.9$ (T02), (c), (d) $A_l = 0.6$ (A16), (e), (f) $A_l = 0.3$ (A13). Solid horizontal line indicates the approximate transition time between the solar-radiation-dominated phase and the convection-dominated phase of RT instability development. Solid arrows are a guide to the eye which indicate the bounds of the character V shape discussed further in the text.

Consequence (1) is the result of decreasing the density difference at the shadow boundary (approximated by $\Delta\rho$) and therefore less lateral motion. Consequence (2) occurs because by decreasing A_l , the temperature under the shadow increases more rapidly, even resulting in RT instabilities in A16 and A13. RT instabilities below the shadow are temporary before the upwelling below the shadow (Fig. 7) is sufficiently large to overcome the temperature difference. These are seen clearly in the temperature field snapshots in Figs. 14(d) and 14(f). At the same time, for $A_l = 0.9$, no RT instabilities form. This suggests that below a certain threshold in A_l the density differences under the shadow are sufficiently large to allow for some net downwards convection, for at least a short time.

As expected, a larger A_l allows the intrusion to propagate further and more rapidly. Up to a propagating distance of 2.5–3 m, the front in A16 propagates very closely to the T02 intrusion, as shown by Fig. 15. The front in A13 propagates even slower. At long times, T02 is able to continue propagating (Fig. 11), whereas the speed of the intrusion in A16 becomes more uncertain, possibly effected by cool plumes reaching the top boundary. In A13, the intrusion slows dramatically, similar to the T03 case in the previous section.

3. Attenuation length

For variations of A_l and T_0 , there is a natural vertical length scale over which to average which is constant across each case: the attenuation length. For comparing La2 and La8, where $\lambda = 0.2$ and 0.4 m, respectively, we continue to use the attenuation length as the depth over which we average the temperature in Fig. 16, but this implies that the region we average over is different for each case. By increasing λ , as is done from Figs. 16(a) to 16(c) to 16(e), we modify the RT instability growth rate in a different way. In T01, T02, T03, A13, and A16, the shape of the forcing term away from the shadow [Eq. (2)] is independent of these parameters. For La2 and La8, not only is the magnitude of

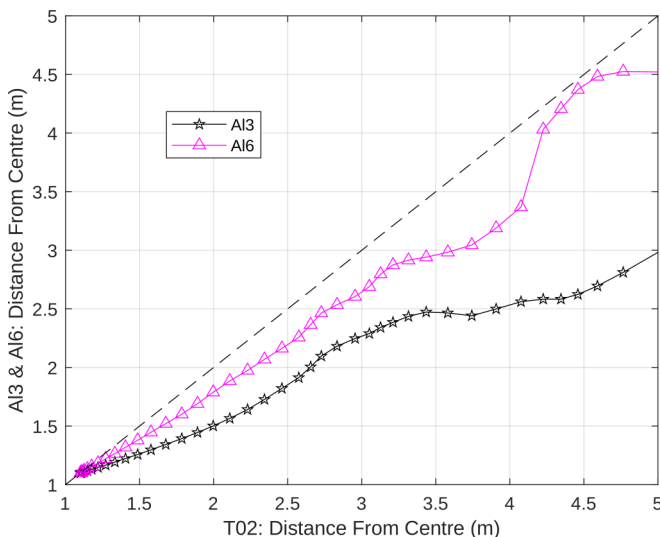


FIG. 15. Intrusion front positions of A13 and A16 as a function of the intrusion front position for the main shadowed system (T02). Symbols are front positions extrapolated from SPINS output separated by a time interval of 60 s, connecting lines are a guide to the eye. If a curve is above the diagonal, dashed line, then it has propagated further than T02 up to that time. If it is below the diagonal line T02 has propagated further over the same time interval. Curves parallel to the diagonal are propagating at the same speed.

forcing at the surface changed, the shape of the Beer-Lambert law forcing is modified at all depths as it is set by the magnitude at the surface. This is illustrated by the dependence of $\Delta\rho$ on λ Fig. 3.

In La2, the temperature forcing is the largest of all cases at the surface and weakest at the mid depths and below. In La8, the temperature forcing is weaker at the surface than all but A13 and T03, but it is the strongest of all cases at the middepths and below. From this analysis, we can expect that RT instabilities should develop quickest in La2 and slowest in La8, forcing a shortened and prolonged solar-radiation-dominated phase, respectively.

The results are consistent with this analysis. The transition to the convection-dominated regime is quickest in La2 [Fig. 16(a)] and slowest in La8 [Fig. 16(e)], with T02 at an intermediate transition time. This effect is especially clear in the right column of Fig. 16, where the boundaries of the RT instabilities are well defined in Fig. 16(b) and nearly nonexistent in Fig. 16(f). A consequence of slower development of the RT instabilities is that the intrusion and return flow are much clearer in the temperature field [Fig. 16(f)].

In addition, a change to λ has only a very small effect on the propagation of an intrusion compared to the other parameters variations in this section (Fig. 17). La8 and T02 both consistently propagate for the entire simulation time and at nearly equal speeds. La2 propagates at a similar rate up to a distance of 3 m from the center, but quickly slows to a stop. This suggests that a sharper gradient in the forcing can cause the intrusion to slow down dramatically. A sufficiently short attenuation length thus appears to be a mechanism by which the intrusion propagation can be arrested.

C. Effect of noise

Instabilities, including RT instabilities, which form due to unstable stratification require small perturbations to provide a seed that grows into macroscopic instabilities observed in simulations (see Sec. III or [40]). In nature, there are endless mechanisms which can generate perturbations: wind, cloud cover, and bathymetry are only a few examples. A low order numerical method introduces perturbations due to truncation error, which can be sufficiently large to grow into instabilities in the flow [41]. In a higher order method, such as that employed by SPINS, the numerical error introduced through the method is much smaller and therefore perturbations must be

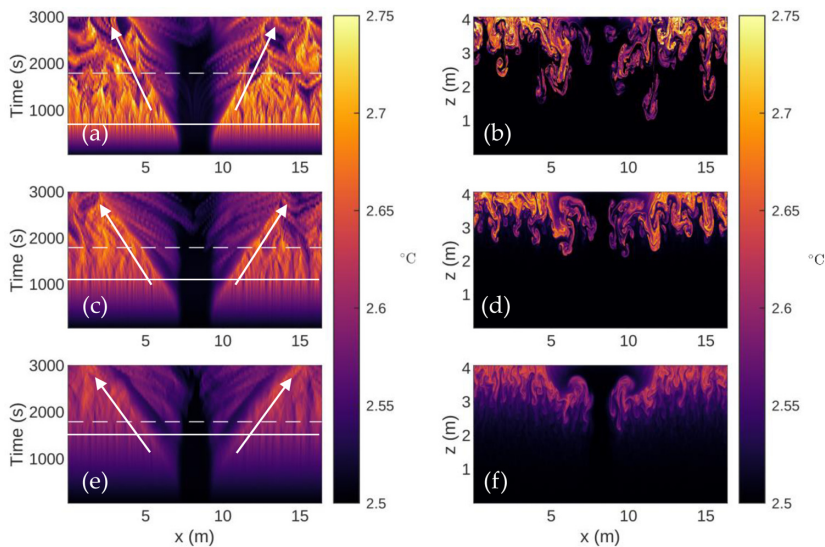


FIG. 16. Averaged and full temperature fields for La2, To2, and La8. (a), (c), (e) Vertically averaged temperature field vs time. Vertical λ . (b), (d), (f) Is the full temperature field at the time indicated by the horizontal dashed line in (a), (c), (e). (a), (b) $\lambda = 0.2$ m (La2), (c), (d) $\lambda = 0.4$ m (TO2), (e), (f) $\lambda = 0.8$ m (La8). Solid horizontal line indicates the approximate transition time between the solar-radiation-dominated phase and the convection-dominated phase of RT instability development. Solid arrows are a guide to the eye which indicate the bounds of the character V shape discussed further in the text.

introduced artificially in order for instabilities to develop in a reasonable simulation time [26,28,42]. Perturbations can also be introduced via an external forcing as in [43,44]. The perturbations can take the form of small variations in temperature or velocity. In the simulations presented in Sec. III, by the nature of the initial conditions (T_0 is a constant) and the forcing [Eq. (2) is a smooth function], additive perturbations were introduced to the temperature field at the initial time.

Without artificial noise, RT instabilities will not develop away from the shadow on the timescale of the simulations, altering the conditions at the intrusion front. RT instabilities are a mechanism which transports heat deposited near the surface, towards the bottom. This is evident in the horizontally averaged temperature field in Fig. 5. In addition, the RT instabilities generate motion near the surface. Unlike a typical gravity current experiment or simulation, the region into which the intrusion propagates is not static. The result of removing noise from the initial conditions is shown in Fig. 18(a). The features of the intrusion on both sides of the shadow are symmetric. The shape of the intrusion front and the eddies generated by the return flow are clearly evident.

This is in stark contrast to the equivalent simulation with noise [Fig. 18(b)]. Noise is introduced to this simulation by assigning a temperature at each grid point randomly selected from a normal distribution with a mean of 2.5 °C and standard deviation of 0.035 . This technique is used for all simulations included in this paper and listed in Table II. The result is a pair of intrusions which are significantly less prominent in the temperature field. Evidence of a significant return flow and a intrusion front are both diminished. The intrusion front position is not as sharply resolved and temperatures in the path of the intrusion are diminished compared in Fig. 18(a).

Despite this shortcoming of the noisy simulations [Fig. 18(a)], the front position is still identifiable and comparable with the noiseless case [Fig. 18(b)]. In Fig. 19 we compare the exact positions of the intrusions with and without noise using the same approach as in Sec. III. For the first ≈ 1200 s, the front position evolves identically between the noisy and noiseless cases. After this period, the noisy case begins to slow compared to the noiseless case. However, the intrusion in the noisy case does not continue to slow down as one might expect. Instead, after a brief period of slowing, it

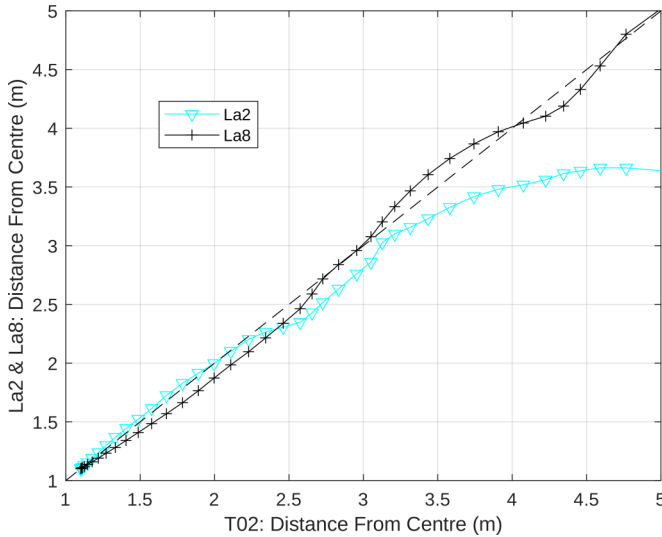


FIG. 17. Intrusion front positions of La2 and La8 as a function of the intrusion front position for the main shadowed system (T02). Symbols are front positions extrapolated from SPINS output separated by a time interval of 60 s, connecting lines are a guide to the eye. If a curve is above the diagonal, dashed line, then it has propagated further than T02 up to that time. If it is below the diagonal line T02 has propagated further over the same time interval. Curves parallel to the diagonal are propagating at the same speed.

resumes propagating at near the same speed as the noiseless case. The distance between the noisy and noiseless cases reaches a maximum at 1800 s of 0.4 m.

The significance of this result is that it shows that an intrusion at the surface due to lateral variations in solar radiation is robust despite changes in the conditions at the intrusion front and changes to the noise introduced at the onset of the simulation. It also demonstrates why finding an

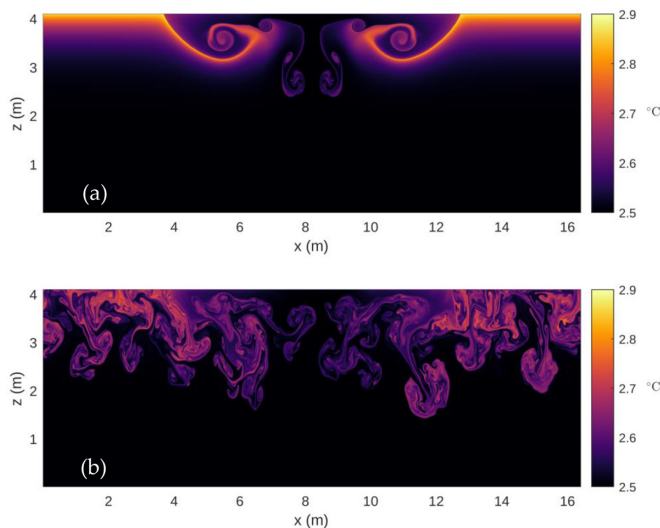


FIG. 18. Intrusion in the temperature field for case T02 at 2100 s with (a) no noise in temperature field at the onset of the simulation and (b) normally distributed noise in the temperature field at the onset of the simulation.

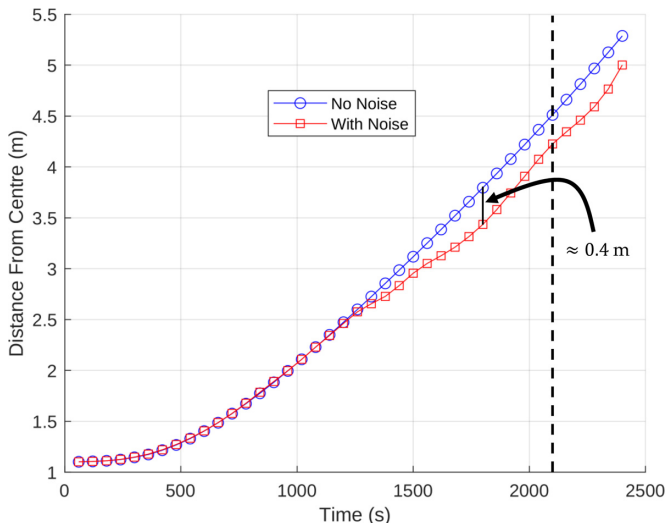


FIG. 19. Position of the intrusion front vs time with and without noise (see legend). Vertical dashed line indicates the time corresponding to Fig. 18. Approximate maximum difference between the intrusion position with and without noise is labeled by the vertical bar at $t = 1800$ s.

approximate front speed is perhaps not a useful approach as the front speed is gradually increasing (most evident in the noiseless case) in both cases as the mean temperature at the current front is increasing. In the noiseless case, temperatures at the intrusion front are warmer and the ambient fluid is motionless. In the noisy case, temperatures at the intrusion front are cooler on average than the noiseless case and there is fluid motion. These differences in temperature and motion are due to the development of the RT instabilities. Despite generally cooler temperatures in the noisy case (due to the mixing enabled by the RT instabilities), the mean density difference at the surface are comparable to the noiseless case. Despite the clear horizontal temperature differences in Fig. 18(b) at the surface due to the formation of RT instabilities, the intrusion is able to propagate to nearly the same distance as the noiseless case. It is thus reasonable to expect that most buoyancy driven flows in an ice-covered, in-land lake would not be sufficiently large to disrupt lateral intrusions like those presented in this paper.

IV. DISCUSSION

As shown in Eq. (11), there are four main parameters which modulate the strength of horizontal buoyancy differences:

- (1) The spatial variations in solar radiation intensity, determined by A_I .
- (2) The rate at which radiation is absorbed in the water column, determined by λ .
- (3) The position on the equation of state relative to the T_{MD} , determined by T_0 .
- (4) The magnitude of the incoming solar radiation, determined by, Q_0 .

The effect of the first three was explored in Sec. III B. In the following discussion, we present relevant measurements of the first three parameters in ice-covered lakes in order to situate the results in Sec. III.

A. Albedo measurements

In this paper, the word albedo (and symbol A_I) was used to describe the magnitude of the spatial changes in solar radiation intensity at the top of the water column. Typically, albedo is reserved as a term for the fraction of radiation reflected at the surface. Due to attenuation inside the ice and snow layers above the water column, albedo—as recorded on ice-covered lakes—is insufficient to

fully characterize the amount of solar radiation that reaches the water column. More accurately, A_l is the magnitude of the spatial changes in the transmissivity, the fraction of radiation that was not absorbed or reflected before reaching the water column. Measurements of the transmissivity ranged between 0.1 and 0.6 in Lake Vendyurshkoe and Lake Onega (Russia) [20,45].

$A_l = 0.9$ was used in several cases (see Table II) and the main system (Sec. III A) would correspond to a transmissivity of 0.1 of lake ice, adjacent to open water which typically has a transmissivity above 0.9. Cases A13 and A16 also fit into this parameter range, with weaker transmissivity on the ice-covered portion. Given that these simulations do not consider wind forcing, further research is needed to quantify the effect of nonuniform solar radiation coupled with wind forcing on the open parts of the surface.

Spatial changes in ice thickness could also have a meaningful effect on spatial changes in solar radiation intensity. However, to our knowledge the spatial variations in solar radiation intensity are seldom measured or linked to changes in ice thickness. The lakes mentioned above, had measured ice thickness ranging from 30–40 cm, with the surface mostly clear of snow [20,45]. In Ref. [45], in the second year data were reported, the transmissivity increased to the larger value of 0.6 in the late winter, which corresponded with a near 40% loss in ice thickness.

Reference [46] showed that snow cover increased albedo measurements over lake ice from ≈ 0.4 to ≈ 0.8 after a snowfall. Spatial variations from clear ice to snow-covered ice can have albedo differences near 0.4. This suggests that by changes in snow cover alone, we can expect significant transmissivity differences. Similarly, in Ref. [32], mean measurements of transmissivity were ≈ 0.4 in 2015 and 2017 while the ice was clear of snow. The authors measured a transmissivity of < 0.1 in 2016, the year when the downwelling solar radiation was most intense [32]. Reference [32] attributes most of the difference to a thin and patchy snow layer of up to 5 cm in depth. One might expect large spatial variations in transmissivity of ≈ 0.35 due to changes in snow cover alone. In Ref. [45] albedo measurements were reported for a wide array of cover: fresh snow (0.8), old snow (0.6), white ice (0.35), congelation ice (0.3), and water on the ice surface (0.15). This shows that by only considering changes in albedo, significant lateral variations in solar radiation intensity can be measured simply by variations in conditions at the surface.

B. Attenuation length measurements

Water clarity is an important parameter in several subdisciplines in the study of inland water bodies [14,47,48]. Irradiance incident on a clear lake will penetrate deep into the water column, with only a small fraction of the radiation absorbed per unit length. A turbid lake will have the opposite effect; a larger fraction of the incident radiation is absorbed per unit length. In this paper, the absorption of incident radiation is modeled using Eqs. (1c) and (2), which assumes that all incoming radiation is absorbed at the same rate with a single attenuation coefficient. This simplifying assumption is appropriate for this process study and is used in other simulations which consider the effects of solar radiation in temperatures below T_{MD} [14,15,35].

Lake Erie and Lake Onega are two large inland lakes with significant ice coverage during the year where measurements of lake clarity and estimates of the attenuation length have been obtained [32,47]. Attenuation lengths were measured in Lake Erie at several specific wave lengths and as an average over the photosynthetically active radiation (PAR) range (approx. 400–700 nm) [47]. The attenuation in the PAR band was measured at four stations with an attenuation length as small as 0.78 m and as large as 1.60 m. The attenuation lengths varied from as low as 0.71 m in the middle of the PAR band, to as high as 4.03 m for the shortest wavelength in the PAR band (see Table 2 in Ref. [47]).

The light attenuation as a function of wavelength over the PAR band was also measured in Lake Onega [32]. The attenuation lengths varied from as low as 0.2 m for ~ 440 nm light to as large as 0.8 m for ~ 700 nm light. The median attenuation length over the PAR band is approximately 0.32 m [see Fig. 5(a) in Ref. [32]; the median is a qualitative estimate and not reported in the paper].

In Sec. III A we start our analysis with an attenuation length of 0.4 m matching the value used in other high-resolution, nonhydrostatic simulations of ice-covered lakes [14,15]. In Sec. III B we

looked at one smaller value of 0.2 m and one larger value of 0.8 m. The parameter range considered here is comparable to those measured in Lake Onega [13] and typical of lakes more turbid than Lake Erie [47].

C. Temperature measurements

Our goal in varying T_0 in this process study was to probe the effect of the nonlinearity of the equation of state on the lateral intrusion that develops due to the shadowed region. Real ice-covered lakes in the late winter develop a stratification with three main layers [11,13]: (1) sharp diffusive layer immediately below the ice, (2) CML which is approximately spatially constant in temperature, and increasing in depth and temperature with time, (3) a stably stratified layer towards the bottom. The sharp diffusive layer comes from the ice cover forcing the top boundary to maintain a temperature of 0°C and is neglected in this process study. The CML is nearly constant in temperature with depth and, therefore, is somewhat comparable to the simulations discussed in Sec. III. CML temperatures in Lake Onega were measured in the range of 0.2°C to 1°C in March over several years, cooler than the simulations discussed in this paper which would result in higher potential for lateral motion, as suggested by Fig. 12. The CML temperatures in Lake Pääjärvi were found to be significantly warmer, up to 2°C , in April [11]. In Ref. [16] the CML is nearly constant in density but not in temperature due to the influence of salinity. However, these measurements show that temperatures near T_{MD} develop near the surface as we approach ice-off [16].

V. CONCLUSIONS

We have presented simulations of a two-dimensional system initially at constant temperature subjected to temperature forcing via the Beer-Lambert Law, with a shadowed region. At the center of this region the solar radiation at the surface is reduced by a factor of A_l . Shadowing leads to lateral buoyancy differences, and after some time, outward moving intrusions are generated at the surface, systematically transporting the cooler fluid under the shadowed region away from the shadow. In response to this outward motion along the surface, a return flow of warmer fluid forms. This fluid, largely consisting of fluid trapped in the finite-sized manifestations of RT instabilities, is transported back towards shadowed region, where it is pushed upwards near the shadow boundary.

In addition to systematic lateral motion, vertical motion was also effected in a systematic way. The effect of the shadowed region on vertical motion was identified using KE_{avg} (Eq. (6)). KE_{avg} [Fig. 9(a)] reveals two distinct regimes in both the shadowed and unshadowed cases, where the shadowed cases transition between regimes at earlier times than their unshadowed counterparts. This earlier transition is due to the enhanced vertical buoyancy flux generated by the lateral motion at the shadow boundary. This is apparent in by the average vertical buoyancy flux per unit mass shown in Fig. 10(a). A shadowed region is a mechanism for lateral transport and transport of warmer fluid towards the bottom. In a system with no shadowed region, the lateral motion is not systematic and the development of RT instabilities is much slower at transporting warmer fluid towards the bottom. It should be noted that the average buoyancy flux per unit mass does eventually catch up to the shadowed case as shown in Fig. 10(a).

The physical parameters which modify the development of the later intrusions are the albedo, A_l , the attenuation length, λ , and the initial temperature, T_0 . The short time effect of each of these parameters can be roughly quantified by the quantity $\Delta\rho$ [Eq. (11)]. $\Delta\rho \propto A_l$ and a larger A_l results in a faster and more robust intrusion along the surface. $\Delta\rho \propto \alpha(T_0)$, where α , the thermal expansion coefficient, is a decreasing function of temperature. As $T_0 \rightarrow T_{MD}$ the density differences for similar temperature differences are decreased resulting in slower development of an intrusion that is less robust.

The dependence on λ is more complicated. Increasing λ both decreases the magnitude of $\Delta\rho$ at the surface and increases the vertical extent of the solar forcing. This results in slower development and increased vertical extent of RT instabilities. Despite these quantifiable changes, the intrusions near the surface appear to develop at a similar rate initially, differing from the

variations to T_0 and A_l (see Figs. 13, 15, and 17). Only the smaller $\lambda = 0.2$ m case produces an intrusion which slowed over the duration of the simulations. $\lambda = 0.4$ and 0.8 m remained similarly robust.

In terms of dimensional variables, we identified variations in the duration of the acceleration phase and the speeds of the intrusion during the propagation phase that depended strongly on A_l , λ , and T_0 . In terms of dimensionless variables, the duration of the acceleration phase and propagation speeds collapsed to a single value, except for the cases where A_l was varied (cases A13 and A16).

The numerical model we use, SPINS, is a high-order pseudospectral model, and as such artificial noise is required in order to seed instabilities, such as the RT instabilities that form away from the shadowed region (see Fig. 4). Naturally one expects that the development of RT instabilities in the region away from the shadow would modulate the lateral intrusions with propagate outward, near the surface. A comparison between the front position of the intrusions in an identical simulation to T02 (see Table II) with the no initial noise revealed that the front position is not as strongly dependent on the development of RT instabilities away from the shadow as initially thought. In the solar-radiation-dominated regime, the effect of noise on the front position was negligible. The intrusion was slowed temporarily shortly after the transition into the convection-dominated regime but propagated at a similar rate thereafter (Fig. 19). This is despite the fact that the intrusion is barely recognizable in the temperature field as in Fig. 18. This shows that the lateral intrusions are a robust feature which depend only very weakly on the surrounding RT instability set conditions.

In Sec. IV measurements of transmissivity, albedo, attenuation length, and temperature in ice-covered lakes are reported to provide context to the simulations presented in this paper. We show that generally, the parameters presented in this paper are plausible in ice-covered lakes, but that this process should be further investigated via field experiments.

In the future, we will extend this research to the following areas: (1) additional configurations of shadowed regions in two-dimensional simulations, (2) systems with preexisting stratification, and (3) three-dimensional simulations.

In this research, we considered only a single shadowed region surrounded by unshadowed regions. There are multiple possibilities for additional configurations. A few possibilities that are of interest include (a) adding a second shadowed region near the first and studying how the intrusions interact, (b) reversing the unshadowed and shadowed region such that the radiation will be shadowed everywhere except a small region in the center, mimicking the effects of a lead or a small region with no snow, and (c) highly variable shadowing with a sinusoidal function driving horizontal oscillations in radiation intensity. Future work with a background stratification would start with a weak and linear stratification similar to what one might expect in the late winter just as the snow melts [11]. Future three-dimensional simulations would be intended to probe the three-dimensional nature of the intrusions which result from horizontal albedo variations. The first natural extension of this work is to extend the two-dimensional system studied in this paper into the third dimension without adjusting the shadow. Another extension that we will explore in future work will be to study a variety of shadow geometries in three dimensions.

ACKNOWLEDGMENTS

This work was supported by NSERC Discovery Grant RGPIN-311844-37157 and computational resources obtained via a resource allocation competition, funded by the Digital Research Alliance of Canada. The authors would like to thank the two anonymous reviewers and the editor whose suggestions have lead to substantial improvements to this paper.

[1] J. J. Magnuson, D. M. Robertson, B. J. Benson, R. H. Wynne, D. M. Livingstone, T. Arai, R. A. Assel, R. G. Barry, V. Card, E. Kuusisto *et al.*, Historical trends in lake and river ice cover in the northern hemisphere, [Science](#) **289**, 1743 (2000).

- [2] C. Verpoorter, T. Kutser, D. A. Seekell, and L. J. Tranvik, A global inventory of lakes based on high-resolution satellite imagery, *Geophys. Res. Lett.* **41**, 6396 (2014).
- [3] R. I. Woolway and C. J. Merchant, Worldwide alteration of lake mixing regimes in response to climate change, *Nat. Geosci.* **12**, 271 (2019).
- [4] D. R. Mueller, P. Van Hove, D. Antoniadou, M. O. Jeffries, and W. F. Vincent, High arctic lakes as sentinel ecosystems: Cascading regime shifts in climate, ice cover, and mixing, *Limnol. Oceanogr.* **54**, 2371 (2009).
- [5] S. Karetnikov, M. Leppäranta, and A. Montonen, A time series of over 100 years of ice seasons on Lake Ladoga, *J. Great Lakes Res.* **43**, 979 (2017).
- [6] M. J. Hewer and W. A. Gough, Lake Ontario ice coverage: Past, present and future, *J. Great Lakes Res.* **45**, 1080 (2019).
- [7] B. Yang, J. Young, L. Brown, and M. Wells, High-frequency observations of temperature and dissolved oxygen reveal under-ice convection in a large lake, *Geophys. Res. Lett.* **44**, 12 (2017).
- [8] C. R. Duguay, G. M. Flato, M. O. Jeffries, P. Ménard, K. Morris, and W. R. Rouse, Ice-cover variability on shallow lakes at high latitudes: Model simulations and observations, *Hydrol. Processes* **17**, 3465 (2003).
- [9] K. B. Winters, P. N. Lombard, J. J. Riley, and E. A. D’Asaro, Available potential energy and mixing in density-stratified fluids, *J. Fluid Mech.* **289**, 115 (1995).
- [10] K. B. Winters, H. N. Ulloa, A. Wüest, and D. Bouffard, Energetics of radiatively heated ice-covered lakes, *Geophys. Res. Lett.* **46**, 8913 (2019).
- [11] G. Kirillin, M. Leppäranta, A. Terzhevik, N. Granin, J. Bernhardt, C. Engelhardt, T. Efremova, S. Golosov, N. Palshin, P. Sherstyankin *et al.*, Physics of seasonally ice-covered lakes: A review, *Aquat. Sci.* **74**, 659 (2012).
- [12] D. M. Farmer, Penetrative convection in the absence of mean shear, *Q. J. R. Meteorol. Soc.* **101**, 869 (1975).
- [13] D. Bouffard and A. Wüest, Convection in lakes, *Annu. Rev. Fluid Mech.* **51**, 189 (2019).
- [14] H. N. Ulloa, K. B. Winters, A. Wüest, and D. Bouffard, Differential heating drives downslope flows that accelerate mixed-layer warming in ice-covered waters, *Geophys. Res. Lett.* **46**, 13872 (2019).
- [15] C. L. Ramón, H. N. Ulloa, T. Doda, K. B. Winters, and D. Bouffard, Bathymetry and latitude modify lake warming under ice, *Hydrol. Earth Syst. Sci.* **25**, 1813 (2021).
- [16] A. Cortés and S. MacIntyre, Mixing processes in small arctic lakes during spring, *Limnol. Oceanogr.* **65**, 260 (2020).
- [17] K. Salonen, M. Pulkkanen, P. Salmi, and R. W. Griffiths, Interannual variability of circulation under spring ice in a boreal lake, *Limnol. Oceanogr.* **59**, 2121 (2014).
- [18] C. R. Ellis, H. G. Stefan, and R. Gu, Water temperature dynamics and heat transfer beneath the ice cover of a lake, *Limnol. Oceanogr.* **36**, 324 (1991).
- [19] D. L. Stefanovic and H. G. Stefan, Two-dimensional temperature and dissolved oxygen dynamics in the littoral region of an ice-covered lake, *Cold Reg. Sci. Technol.* **34**, 159 (2002).
- [20] D. Bouffard, R. E. Zdrovennov, G. E. Zdrovennova, N. Pasche, A. Wüest, and A. Y. Terzhevik, Ice-covered Lake Onega: Effects of radiation on convection and internal waves, *Hydrobiologia* **780**, 21 (2016).
- [21] M. Leppäranta, *Freezing of Lakes and the Evolution of Their Ice Cover* (Springer Science & Business Media, Berlin, Heidelberg, 2014).
- [22] H. N. Ulloa, G. Constantinescu, K. Chang, D. Horna-Munoz, Océane Hames, and A. Wüest, Horizontal transport under wind-induced resonance in stratified waterbodies, *Phys. Rev. Fluids* **5**, 054503 (2020).
- [23] A. L. Forrest, B. E. Laval, R. Pieters, and D. S. S. Lim, Convectively driven transport in temperate lakes, *Limnol. Oceanogr.* **53**, 2321 (2008).
- [24] A. A. Zhdanov, R. Y. Gnatovskii, N. G. Granin, V. V. Blinov, I. A. Aslamov, and V. V. Kozlov, Variations of under-ice currents in Southern Baikal by data of 2012–2016, *Water Resour.* **44**, 442 (2017).
- [25] C. J. Subich, K. G. Lamb, and M. Stastna, Simulation of the Navier–Stokes equations in three dimensions with a spectral collocation method, *Int. J. Numer. Methods Fluids* **73**, 103 (2013).
- [26] C. Xu, M. Stastna, and D. Deepwell, Spontaneous instability in internal solitary-like waves, *Phys. Rev. Fluids* **4**, 014805 (2019).

- [27] A. Grace, M. Stastna, and F. J. Poulin, Numerical simulations of the shear instability and subsequent degeneration of basin scale internal standing waves, *Phys. Rev. Fluids* **4**, 014802 (2019).
- [28] A. P. Grace, M. Stastna, K. G. Lamb, and K. A. Scott, Asymmetries in gravity currents attributed to the nonlinear equation of state, *J. Fluid Mech.* **915**, A18 (2021).
- [29] S. Legare, A. Grace, and M. Stastna, Double-diffusive instability in a thin vertical channel, *Phys. Fluids* **33**, 114106 (2021).
- [30] D. Brydon, S. Sun, and R. Bleck, A new approximation of the equation of state for seawater, suitable for numerical ocean models, *J. Geophys. Res.: Oceans* **104**, 1537 (1999).
- [31] J. A. Colman and D. E. Armstrong, Horizontal diffusivity in a small, ice-covered lake, *Limnol. Oceanogr.* **28**, 1020 (1983).
- [32] D. Bouffard, G. Zdrovennova, S. Bogdanov, T. Efremova, S. Lavanchy, N. Palshin, A. Terzhevik, L. R. Vinnå, S. Volkov, A. Wüest *et al.*, Under-ice convection dynamics in a boreal lake, *Inland Waters* **9**, 142 (2019).
- [33] P. K. Kundu and I. M. Cohen, *Fluid Mechanics* (Academic Press, Philadelphia, 1990).
- [34] H. N. Ulloa, C. L. Ramón, T. Doda, A. Wüest, and D. Bouffard, Development of overturning circulation in sloping waterbodies due to surface cooling, *J. Fluid Mech.* **930**, A18 (2022).
- [35] A. P. Grace, M. Stastna, K. G. Lamb, and K. A. Scott, Numerical simulations of the three-dimensionalization of a shear flow in radiatively forced cold water below the density maximum, *Phys. Rev. Fluids* **7**, 023501 (2022).
- [36] V. Bouillaut, S. Lepot, S. Aumaître, and B. Gallet, Transition to the ultimate regime in a radiatively driven convection experiment, *J. Fluid Mech.* **861**, R5 (2019).
- [37] A. Dai and C.-S. Wu, High-resolution simulations of cylindrical gravity currents in a rotating system, *J. Fluid Mech.* **806**, 71 (2016).
- [38] B. Yang, M. G. Wells, B. C. McMeans, H. A. Dugan, J. A. Rusak, G. A. Weyhenmeyer, J. A. Brenttrup, A. R. Hrycik, A. Laas, R. M. Pilla *et al.*, A new thermal categorization of ice-covered lakes, *Geophys. Res. Lett.* **48**, e2020GL091374 (2021).
- [39] D. E. Kelley, Convection in ice-covered lakes: Effects on algal suspension, *J. Plankton Res.* **19**, 1859 (1997).
- [40] J. Olsthoorn, E. W. Tedford, and G. A. Lawrence, Diffused-interface Rayleigh-Taylor instability with a nonlinear equation of state, *Phys. Rev. Fluids* **4**, 094501 (2019).
- [41] M. F. Barad and O. B. Fringer, Simulations of shear instabilities in interfacial gravity waves, *J. Fluid Mech.* **644**, 61 (2010).
- [42] O. B. Fringer, M. Gerritsen, and R. L. Street, An unstructured-grid, finite-volume, nonhydrostatic, parallel coastal ocean simulator, *Ocean Modell.* **14**, 139 (2006).
- [43] K. G. Lamb and D. Farmer, Instabilities in an internal solitary-like wave on the Oregon Shelf, *J. Phys. Oceanogr.* **41**, 67 (2011).
- [44] P.-Y. Passaggia, K. R. Helfrich, and B. L. White, Optimal transient growth in thin-interface internal solitary waves, *J. Fluid Mech.* **840**, 342 (2018).
- [45] M. Leppäranta, A. Terzhevik, and K. Shirasawa, Solar radiation and ice melting in Lake Vendyurskoe, Russian Karelia, *Hydrol. Res.* **41**, 50 (2010).
- [46] N. A. Svacina, C. R. Duguay, and L. C. Brown, Modelled and satellite-derived surface albedo of lake ice—Part I: Evaluation of the albedo parameterization scheme of the Canadian lake ice model, *Hydrol. Proc.* **28**, 4550 (2014).
- [47] M. R. Twiss, R. M. L. McKay, R. A. Bourbonniere, G. S. Bullerjahn, H. J. Carrick, R. E. H. Smith, J. G. Winter, N. A. D'souza, P. C. Furey, A. R. Lashaway *et al.*, Diatoms abound in ice-covered Lake Erie: An investigation of offshore winter limnology in Lake Erie over the period 2007 to 2010, *J. Great Lakes Res.* **38**, 18 (2012).
- [48] B. Yang, M. G. Wells, J. Li, and J. Young, Mixing, stratification, and plankton under lake-ice during winter in a large lake: Implications for spring dissolved oxygen levels, *Limnol. Oceanogr.* **65**, 2713 (2020).

Correction: The previously published Figure 10 was not the final version of the figure and has been replaced with the correct version.